Thermal Conductivity Measurements Using the 3-Omega Technique:

Application to Power Harvesting Microsystems

By
David de Koninck

Department of Mechanical Engineering
McGill University
Montréal, Canada

Thesis submitted to McGill University in partial fulfillment of the requirements
for the degree of Master of Engineering

Under the joint supervision of:

Professor Srikar Vengallatore
Department of Mechanical Engineering
McGill University
And
Professeur Luc Fréchette
Département de Génie Mécanique
Université de Sherbrooke

August 2008

“The most exciting phrase to hear in science, the one that heralds the most discoveries, is not 'Eureka!' but 'That's funny'”

Isaac Asimov

Abstract

The optimal design of power generating microsystems requires accurate knowledge of the thermal properties of their constituent materials at the appropriate length scale. The goal of this thesis was to build an apparatus for measuring the thermal conductivity of thermally-insulating dielectric materials using the so-called 3-omega technique. This technique utilizes a microfabricated metal line deposited on the specimen to act as a resistive heater. When an alternating current (AC) voltage signal is used to excite the heater at a frequency ω, the periodic heating generates oscillations in the electrical resistance of the metal line at a frequency of 2ω. In turn, this leads to a third harmonic (3ω) in the voltage signal, which is used to infer the magnitude of the temperature oscillations. The frequency dependence of these oscillations can be analyzed to obtain the thermal properties of the specimen.

The device consisted of a voltage source, a custom-built analog circuit and sample mount, a lock-in amplifier. The sample was placed within a vacuum chamber and evacuated using a made-to-order vacuum system. Personalised LabVIEW and MATLAB programs were created for autonomous data acquisition and analysis.

The 3ω technique is simple, quick and accurate; tests using a standard fused quartz specimen ($k = 1.38 \pm 0.04$ W/m·K) yielded a measured thermal conductivity of 1.47±0.16 W/m·K. Subsequently, the technique was used to measure the thermal conductivity of Lead Zirconate Titanate (PZT-5A4E), which is a piezoelectric ceramic of interest for integration with microfabricated vibration energy harvesters. This material was found to exhibit a low thermal conductivity of 1.38±0.10 W/m·K.

Résumé

Le design optimal de microsystèmes pour la génération d'énergie demande une connaissance précise des propriétés thermiques des matériaux utilisés, à la bonne échelle. Le but de ce projet fut de créer un instrument pour mesurer la conductivité thermique des matériaux fonctionnels pour ces microsystèmes en utilisant la méthode 3-oméga. Cette méthode se sert d'une ligne métallique déposée en surface qui agit comme élément chauffant. Quand le filament métallique est alimenté par un courant alternatif (CA) à une fréquence ω, la puissance dissipée par effet Joule génère une oscillation sinusoïdale dans la résistance électrique à une fréquence 2ω. Cette résistance électrique sinusoïdale à son tour crée une harmonique de rang 3 (3ω) dans la tension électrique de l'élément chauffant. Cette harmonique est utilisée pour déduire l'amplitude des oscillations de température dans le spécimen. La variation de ces oscillations thermiques en fonction de la fréquence d'excitation nous permet d'obtenir la conductivité thermique de l'échantillon.

L'instrument consiste d'une source de tension, un « lock-in amplifier », un circuit analogique et une monture à échantillon personnalisés. L'échantillon fut placé dans une chambre à vide et évacué à l'aide d'un système à vide fait sur mesure. Des programmes LabVIEW et MATLAB fut écrits pour réaliser l'acquisition et l'analyse de donnés automatisées.

La méthode 3ω est facile à réaliser et donne des résultats précis : des tests avec des échantillons de quartz amorphe (k = 1.38±0.04 W/m·K) ont donné une conductivité thermique de 1.47±0.16 W/m·K. Le quartz amorphe fut utilisé comme référence pour valider l'instrument. Par la suite, l'appareil fut utilisé pour caractériser une céramique PZT (Titano-Zirconate de Plomb), un matériau piézoélectrique souvent utilisé dans la fabrication de microgénérateurs pour la

récupération d’énergie vibratoire. Une conductivité thermique de 1.38±0.10 W/m·K fut mesuré pour le PZT-5A4E.

Acknowledgements

First of all, I would like to thank both of my supervisors, Prof. Srikar Vengallatore and Prof. Luc Fréchette for trusting me throughout my masters and giving me the freedom to learn from my (many) mistakes. It came down to the wire, but the project was a success and I have grown a great deal as a researcher because of them.

I much also acknowledge all of the assistance I received in fabricating and characterizing the specimen heaters at McGill microfabrication facility, particularly Vito Logiudice, Don Berry and Dr. Matthieu Nannini as well as Jean Beerens at the University of Sherbrooke cleanroom.

Special thanks go to Fred Nabki for all his help with electronics related issues. I would also like to thank all the members of the FDA015 for making my graduate studies at McGill memorable. In particular, I would like to thank Guruprasad Sosale, Meysam Rahmat, Jonathan Laliberté, Hassan Shahriar and Sairam Prabhakar for stimulating discussions and help during my masters.

Finally, I must thank my family for their unwavering support during the course of my studies: living away from home made me realize how much their love and support mean to me.

This project would not have been possible without the financial support provided by the masters' research bursary from the Fonds de recherche sur la nature et les technologies (FQRNT) as well as funds from the Natural Sciences and Engineering Council of Canada (NSERC) and General Motors Canada (GMC).

Table of Contents

List of Figures

List of Tables

List of Variables

Latin Alphabet

A	Slope of the linear regression curve
$\hat{A}$	Slope of the linear regression curve, estimate
A_s	Surface area $\left(\mathrm{m}^2\right)$
$A_{xs,s}$	Cross-sectional area of specimen $\left(\mathrm{m}^2\right)$
B	Y-intercept of the linear regression curve
$\hat{B}$	Y-intercept of the linear regression curve, estimate
C_p	Volumetric heat capacity $\left(\mathrm{J/m^3 \cdot K}\right)$
$F_{1-\alpha,\nu_1,\nu_2}$	F-distribution
F^*	Value of random variable following an F-distribution
$I(t)$	Current (A)
$I_h(t)$	Heater current (A)
I_0	Peak amplitude of current (A)
$I_{h,0}$	Peak amplitude of room temperature (nominal) heater current (A)
$I_{h,rms}$	Rms amplitude of room temperature (nominal) heater current (A)
L	Distance (m)
N	Number of sampled points used to determine the regression curve
$P(t)$	Power (W)
$P_{AC}(t)$	Oscillating component of power (W)
P_{DC}	Time-invariant component of power (W)
$\overline{P}$	Average power (W)
P_{rms}	Rms power (W)
Q	Heat Flux (W)
$R(t)$	Electrical resistance (Ω)
$R_h(t)$	Heater electrical resistance (Ω)
R_0	Room temperature (nominal) electrical resistance (Ω)
R_1	In-series Wheatstone bridge electrical resistance (Ω)
R_2	Parallel Wheatstone bridge electrical resistance (Ω)
R_v	Variable Wheatstone bridge electrical resistance (Ω)

$R_{h,0}$	Room temperature (nominal) heater electrical resistance (Ω)
ROR	Low-pass filter roll-off rate $(\mathrm{dB/dec})$
S_{xx}	X sum of squares, $\sum_{i=1}^{N}(x_i - \bar{x})^2$
S_{yy}	Y sum of squares, $\sum_{i=1}^{N}(y_i - \bar{y})^2$
$S_{\hat{y}\hat{y}}$	Regression line sum of squares, $\sum_{i=1}^{N}(\hat{y}_i - \bar{\hat{y}})^2$
S_{xy}	Mixed sum of squares, $\sum_{i=1}^{N}(x_i - \bar{x})(y_i - \bar{y})$
ΔT	Spatial evolution of the steady-state temperature difference (K)
ΔT_{AC}	Spatial evolution of the oscillating component of the steady-state temperature difference (K)
ΔT_{DC}	Spatial evolution of the time-invariant component of the steady-state temperature difference (K)
T_0	Spatial evolution of the room (nominal) temperature (K)
$V(t)$	Electrical potential difference (V)
$V_h(t)$	Heater electrical potential difference (V)
V_0	Peak amplitude room temperature (nominal) electrical potential difference (V)
$V_{h,0}$	Peak amplitude room temperature (nominal) heater electrical potential difference (V)
$V_{h,rms}$	Rms heater electrical potential difference (V)
V_{ω}	Peak amplitude electrical potential difference at the fundamental frequency (V)
$V_{n\omega}$	Peak amplitude electrical potential difference of the nth harmonic (V)
$V_{h,\omega}$	Peak amplitude heater electrical potential difference at the fundamental frequency (V)
$V_{h,3\omega}$	Peak amplitude heater electrical potential difference at the third harmonic (V)
W	Wheatstone bridge output (V)
W_{ω}	Peak amplitude Wheatstone bridge output at the fundamental frequency (V)
$W_{3\omega}$	Peak amplitude Wheatstone bridge output at the third harmonic (V)
b_h	Heater half-width (m)

c_1, c_2	Constants
e	Thermal effusivity, a.k.a. thermal inertia, $\sqrt{kC_p}$ $\left(\text{Jm}^{-2}\text{K}^{-1}\text{s}^{-1/2}\right)$
f_c	Low-pass filter cut-off frequency (Hz)
k	Thermal conductivity $(\text{W/m} \cdot \text{K})$
$k_{//}$	Thermal conductivity, normal direction $(\text{W/m} \cdot \text{K})$
l	Length (m)
l_h	Length of heater (m)
p	Power per unit heater length (W/m)
p_{rms}	Rms power per unit heater length (W/m)
$\tilde{p}_{rms}$	Rms power per unit heater area, $P_{rms}/2bl$ $\left(\text{W/m}^2\right)$
q	Thermal wavenumber $\left(\text{m}^{-1}\right)$
r	Radius (m)
s_A	Y-intercept sample standard deviation
s_B	Slope sample standard deviation
s_ε	Error sample standard deviation
t	Time (s)
t_h	Heater thickness (m)
t_s	Specimen thickness (m)
x, y	Cartesian coordinates (m)
x_i, y_i	Sample paired data
$\bar{x}, \bar{y}$	Mean of sample paired data
$\hat{y}$	Linear regression curve

Greek Alphabet

$\Phi(r,t)$	Temperature (K)
Φ_0	Initial temperature, equivalent to T_0 (K)
$\Delta\Phi_{AC}(r,t)$	Oscillating steady-state temperature difference (K)
$\Delta\Phi_{DC}(r)$	Time invariant steady-state temperature difference (K)
I_0	Modified Bessel function of the first kind
K_0	Modified Bessel function of the second kind
$\Theta(t)$	Temporal evolution of temperature
α	Thermal diffusivity $\left(\text{m}^2/\text{s}\right)$
β	Temperature coefficient of resistance $\left(\text{K}^{-1}\right)$
β_h	Heater temperature coefficient of resistance $\left(\text{K}^{-1}\right)$

δ	Dirac delta function
ε	Regression line error, $y_i - \hat{y}$
ϕ	Phase angle (rad)
η	Wavenumber (m^{-1})
λ	Thermal penetration depth (m)
ρ_{xy}	Correlation coefficient between random variables x and y
ρ_{xy}^2	Coefficient of determination between x and y
σ	Population standard deviation
τ	Period of oscillation (s)
τ_F	Low-pass filter time constant (s)
τ_D	Thermal-diffusion time (s)
$\tau_{F,min}$	Minimum filter time constant needed for a given attenuation (s)
ω	Angular frequency $(\mathrm{rad/s})$
ω_D	Thermal-diffusion angular frequency $(\mathrm{rad/s})$
ξ	Fitting parameter, linear regime approximation

Subscripts

0	Room temperature (nominal)
AC	Oscillating
DC	Time-invariant
F	Filter
e	Regression line error, $\hat{y} - y_i$
h	Heater
n	Higher harmonic
p	Peak amplitude
rms	Root mean squared amplitude
s	Specimen
α	Level of significance
ν_1, ν_2	Degrees of freedom
ω	Peak amplitude, fundamental frequency
3ω	Peak amplitude, third harmonic
$n\omega$	Peak amplitude, nth harmonic
x	In-phase
y	Out-of-phase
$//$	Normal direction

Chapter 1: Introduction

Microsystems are small integrated devices that contain components which range in size from the sub-micrometer to the millimeter level. Such systems are made using fabrication techniques borrowed from the microelectronics industry. As such, the primary building material for microsystems remains single-crystal silicon. Historically, microsystems have combined electronic devices with miniaturized mechanical components—such as beams, diaphragms and springs—to form micro-electro-mechanical systems, or MEMS. Today, a plethora of new microsystems are being developed incorporating a variety of functional ceramic materials with unique properties. Of particular interest in this thesis are piezoelectric ceramics, which can convert mechanical strain into an electrical potential difference. Such materials are being incorporated into microsystems in order to generate electrical power from ambient mechanical vibrations (Priya 2007).

1.1 Power Harvesting Microsystems

Power harvesting microsystems encompass a variety of different power generating MEMS, each tailor-made to convert a different type of ambient energy, such as vibrations, light or waste heat (Roundy et al. 2004). Power harvesting is a particularly appealing approach for meeting the energy demands of wireless sensor networks that are currently being developed for applications in environmental monitoring, structural health monitoring and patient monitoring.

Coupling power harvesting microsystems with wireless sensor nodes would thus enable completely autonomous operation of such networks, without the need for manual recharging or replacement of electrochemical batteries.

However, the performance of the state-of-the-art power harvesting microsystems is far from optimal. Optimizing these devices will require advances in many areas of science and engineering, such as access to accurate material property data, including thermal properties, *at the appropriate length scale*. In particular, accurate characterization of the thermal conductivity (*k*) of insulating ceramic materials as functions of processing conditions and length scale is essential for the design of micro engines, micro fuel cells, and vibration energy harvesters. This area of research has been largely ignored to-date, which motivates the work presented here to characterize low-*k* piezoelectric materials.

1.2 Techniques for Measuring Thermal Conductivity

In this section, we will describe the most popular methods used to measure the thermal conductivity of low thermal conductivity ceramic materials at both large and small scales.

1.2.1 Absolute Plate Method

The absolute plate method is the conventional technique for measuring the thermal conductivity of thermally insulating solid specimens (Touloukian 1973). A constant power source is applied to one side of a thin specimen of a known geometry. If the lateral dimensions of the specimen are much larger than its thickness, then the temperature profile within the specimen is quasi-one-dimensional (quasi-1D) near the centre. Using thermocouples on either side of the specimen, the equilibrium normal temperature difference is measured. Finally, Fourier's Law of heat conduction is used to extrapolate the normal thermal conductivity of the material as

$$k_{//} = -\frac{Q \cdot t_s}{A_{xs,s} \cdot \Delta T}, \tag{1.1}$$

where Q is the input power, ΔT is the normal temperature difference, and t_s and $A_{xs,s}$ are the thickness and cross-sectional area of the specimen, respectively.

There are a number of difficulties involved with this measurement technique. First, a low thermal conductivity material inherently requires more time to reach thermal equilibrium, sometimes requiring several hours to several days. This equilibration time can be reduced by applying a smaller input power and by reducing the thickness of the specimen.

Second, low thermal conductivity materials naturally resist the transport of heat; therefore, a large portion of the applied power can be lost from the surface of the material via radiation or convection. To mitigate these losses, the input power and specimen surface area are reduced.

In the end, we need to reduce all of the parameters in (1.1); therefore, the thermal conductivity obtained using the conventional technique tends to be dominated by measurement errors.

All of these difficulties can be traced back to the fact that the entire specimen is heated to setup a steady, quasi-1D temperature profile. The 3-omega technique overcomes these difficulties by limiting the heat-affected region within the specimen.

1.2.2 3-Omega Technique

Originally, the 3-omega (3ω) technique was developed to measure the thermal diffusivity of metal filaments used in incandescent light bulbs (Corbino 1912). The goal was to understand the short observed lifetimes of metal filament lamps compared to carbon filament ones due to burnout (Ebeling 1908). Later, the method was applied to measure the thermal diffusivity of liquids (Birge and Nagel 1987) and dielectric solids (Moon et al. 1996) by indirectly heating the specimen using a thin *planar* metal filament as both a heater and thermometer in thermal contact with the solid of interest.

The first reported use of the 3ω method to measure the thermal conductivity of solids was by Cahill (Cahill and Pohl 1987). Cahill's 3ω technique—from now on simply referred to as the 3ω technique—utilizes a microfabricated metal *line* deposited on the specimen to act as a heater/thermometer. When an alternating current (AC) voltage signal is used to excite the heater at a frequency ω, the periodic heating generates oscillations in the electrical resistance of the metal line at a frequency of 2ω. In turn, this leads to a third harmonic (3ω) in the voltage signal, which is used to infer the magnitude of the temperature oscillations (Corbino 1911). The frequency dependence of the oscillation amplitude and phase can be analyzed to obtain the thermal conductivity of the specimen.

The 3ω technique greatly reduces the heat-affected region since the magnitude of the temperature oscillations decay exponentially away from the resistive line heater (Cahill and Pohl 1987). Furthermore, equilibration times are drastically reduced because the magnitude of the temperature oscillations reaches dynamic equilibrium within a few cycles of oscillation.

This technique has previously been used to measure the thermal conductivity of a wide variety of materials, including various dielectrics (Cahill 1990; Lee and Cahill 1997), porous specimens (Gesele et al. 1997) and nanostructured materials, such as carbon nanotubes (Hu et al. 2006), and is well suited for characterising low-*k* materials used in MEMS.

1.2.3 Time Domain Thermo-Reflectance

Another technique that is commonly used is time-domain thermoreflectance (TDTR). TDTR uses picosecond laser pulses to locally heat the surface of the specimen (Paddock and Eesley 1986; Chu et al. 2001). The short pulses locally deposit a small amount of energy in the specimen. The surface temperature of the specimen is inferred from the change in reflectance of the surface, which—in the limit of small temperature changes—is linearly dependent on the temperature of the specimen. A second, low power probe laser is used to detect changes in the reflectivity of the material.

The advantage of this technique is that the thermal penetration depth can be limited to tens of nanometers, given a short enough heating pulse, thus enabling direct measurement of thin-film specimens commonly used in microsystems. On the other hand, TDTR measures the thermal diffusivity of the specimen; the thermal conductivity can be inferred given the volumetric heat capacity of the specimen. Furthermore, the laser and optical equipment required for TDTR make this a relatively costly technique. For these reasons, the TDTR technique was not pursued further.

1.3 Goal and Structure of Thesis

The goal of this thesis is to design, instrument, and validate an apparatus for measuring the thermal conductivity of low-*k* materials using the 3ω technique, and to demonstrate the utility of this method by measuring the thermal conductivity of one specific piezoelectric ceramic, namely, Lead Zirconate Titanate (PZT), used in vibration energy harvesters.

This thesis is organized as follows. Chapter 2 provides a detailed discussion of the theoretical considerations underlying the 3ω method and presents the analytical relations used to deduce the thermal conductivity of the specimen. Chapter 3 outlines the different processing steps used to create the microfabricated line heaters as well as the electrical interface between the specimen and the electronic measurement equipment. Chapter 4 presents the experimental apparatus and the details of the experimental procedure. Next, the apparatus was validated using a fused quartz reference specimen. Chapter 5 also presents the details of the data and error analyses. Chapter 6 outlines the results for Lead Zirconate Titanate (PZT-5A4E) and compares the measured thermal conductivity with data found in the literature. Finally, Chapter 7 summarises the findings of this work and elaborates on pertinent future work.

Chapter 2: Theoretical Considerations

The 3ω measurement technique uses a metal filament deposited on a specimen (Figure 2.1) which acts simultaneously as a *resistance heater* and *resistance thermometer detector* (RTD) by passing an *alternating current* (AC) signal through it (Cahill 1990).

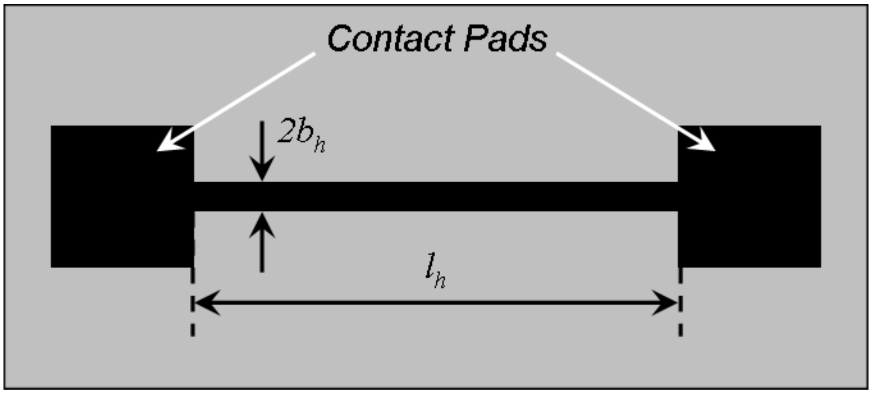

Figure 2.1: Schematic of the metal line filament deposited on a specimen (grey shaped region) used for the 3ω measurements. l_h and b_h denote the heater length and half-width respectively. The contact pads are used to make electrical contact with the microfabricated heater.

An RTD determines the equilibrium temperature of a specimen by measuring the change in resistance of a metal filament in thermal contact with the specimen (Michalski et al. 2001). For small temperature changes, the resistance of the filament varies with temperature as

$$R = R_0\left(1 + \beta\Delta T\right), \tag{2.1}$$

where β is the temperature coefficient of resistance (TCR), and R_0 and R are the resistances at temperatures T_0 and $T_0 + \Delta T$, respectively. Since the TCR for most metals is on the order of 10^{-3} K^{-1}, a Wheatstone bridge is used to measure the minute changes in resistance by passing a *direct current* (DC) signal through the RTD. The amplitude of the DC signal is kept small to minimize any spurious heating from the RTD itself. Alternatively, the RTD can be used as a both a resistive heater and a temperature sensor if a large amplitude signal is used—which will be the strategy pursued in this work.

Given that steady-state temperature measurements of low thermal conductivity specimens are plagued with long equilibration times and large radiation losses, it is preferable to conduct a *transient measurement* using an *alternating current* (AC) excitation signal. As such, an AC signal is passed through the RTD, which acts as both a heater and a thermometer. The power dissipated by the heater/RTD—from now on referred to simply as the heater—due to Joule heating is defined as

$$P = I_h^2 R_h , \tag{2.2}$$

where I_h and R_h are the heater current and resistance respectively. The alternating current passing through the heater is given as

$$I_h(t) = I_{h,0}\cos(\omega t), \tag{2.3}$$

where $I_{h,0}$ is the peak amplitude of the nominal heater current at a frequency ω. Assuming that the change in resistance is negligible compared to the amplitude of the current, the instantaneous power can be written as

$$P(t) = \tfrac{1}{2} I_{h,0}^2 R_{h,0}\left(1 + \cos(2\omega t)\right). \tag{2.4}$$

where $R_{h,0}$ is the nominal heater resistance. As such, the power can be separated into two components: a constant component independent of time and an oscillating component:

$$P_{DC} = \tfrac{1}{2} I_{h,0}^2 R_{h,0} \tag{2.5}$$

$$P_{AC}(t) = \tfrac{1}{2} I_{h,0}^2 R_{h,0}\cos(2\omega t). \tag{2.6}$$

From (DeCarlo and Lin 1995), the average power dissipated by the heater over one cycle is defined as

$$\overline{P} = \frac{1}{\tau}\int_0^{\tau} P(t)dt = \tfrac{1}{2} I_{h,0}^2 R_{h,0}\left(\frac{\omega}{2\pi}\int_0^{2\pi/\omega}\left(1 + \cos(2\omega t)\right)dt\right) = \tfrac{1}{2} I_{h,0}^2 R_{h,0} = P_{DC} . \tag{2.7}$$

The average power dissipated by the heater is also called the root mean square (rms) power, which is half of the power dissipated by a DC current of the same amplitude. Notice that the oscillating component of the instantaneous power *does not* dissipate any average power over one cycle. This will be important later when we discuss the frequency response of the 3ω voltage.

The rms power can also be defined as

$$P_{rms} = I_{h,rms}^2 R_{h,0}, \tag{2.8}$$

where the rms heater current is given by

$$I_{h,rms} = \sqrt{\frac{1}{\tau}\int_0^{\tau} I_h^2(t)dt} = I_{h,0}\sqrt{\frac{\omega}{2\pi}\int_0^{2\pi/\omega}\cos^2(\omega t)dt} = \frac{I_{h,0}}{\sqrt{2}}. \tag{2.9}$$

Assuming that the heater circuit is stable, i.e., that all the transient perturbations decay over time, the steady-state harmonic temperature oscillations in the metal filament produce harmonic variations in the resistance given by (Banerjee et al. 1999) as

$$R_h(t) = R_{h,0}\left(1 + \beta_h \Delta T_{DC} + \beta_h |\Delta T_{AC}| \cos(2\omega t + \phi)\right) \tag{2.10}$$

where $R_{h,0}$ is the nominal (room temperature) resistance of the heater, ΔT_{DC} is the steady-state temperature increase due to the rms power dissipated by the filament, $|\Delta T_{AC}|$ is the magnitude of the steady-state temperature oscillations due to the sinusoidal component of the power and ϕ is the phase angle between the temperature oscillations and the excitation current. The resulting voltage across the sensor is obtained by multiplying the input current be the heater resistance yielding

$$V_h(t) = I_{h,0}R_{h,0}\begin{bmatrix}(1 + \beta_h \Delta T_{DC})\cos(\omega t) + \tfrac{1}{2}\beta_h |\Delta T_{AC}|\cos(\omega t + \phi) \\ + \tfrac{1}{2}\beta_h |\Delta T_{AC}|\cos(3\omega t + \phi)\end{bmatrix}. \tag{2.11}$$

The voltage component at 3ω results from the multiplication of the oscillating current with the periodic portion of the heater resistance at 2ω. From (2.11), one is able to infer the in-phase and out-of-phase components of the temperature oscillations by measuring the voltage signal at the 3ω frequency (Cahill 1990; Cahill 2002):

$$V_{h,3\omega} = \tfrac{1}{2} V_{h,0} \beta_h \Delta T_{AC} , \tag{2.12}$$

where

$$\begin{aligned} V_{h,0} &= I_{h,0} R_{h,0} \\ V_{h,3\omega} &= V_{h,3\omega,x} + i V_{h,3\omega,y} \\ \Delta T_{AC} &= \Delta T_{AC,x} + i \Delta T_{AC,y} \end{aligned}$$

and

$$\begin{aligned} \Delta T_{AC,x} &= \left|\Delta T_{AC}\right| \cos(\phi) \\ \Delta T_{AC,y} &= \left|\Delta T_{AC}\right| \sin(\phi) \end{aligned} .$$

Both the magnitude and phase of the temperature oscillations vary with excitation frequency, due to the *finite* thermal-diffusion time (τ_D) of the specimen. The thermal-diffusion time required for a thermal wave to propagate a distance L is given by (Birge 1986) as

$$\tau_D = L^2 / \alpha , \tag{2.13}$$

where α is the thermal diffusivity, which is defined as the ratio of thermal conductivity (k) to volumetric heat capacity (C_p). In turn, the thermal-diffusion *angular frequency* is

$$\omega_D = \frac{2\pi}{\tau_D} = \frac{2\pi\alpha}{L^2} \propto \alpha . \tag{2.14}$$

In the limit of infinite thermal diffusivity (i.e., infinite thermal conductivity), heat propagates with infinite velocity such that the temperature is constant throughout the specimen. This leads to undamped temperature oscillations with zero phase lag. Conversely, zero thermal diffusivity (i.e., infinite volumetric heat capacity), results in no heat propagation, zero oscillation amplitude, and large phase lag. Note that the dissipation of the rms power is independent of the frequency response of the specimen since it is constant with time.

Next, the heat equation will be solved to determine the values of ΔT_{DC}, $\left|\Delta T_{AC}\right|$ and ϕ for a given input power. In order to construct a mathematical model for a finite width line heater deposited on the surface of the specimen, it is useful to begin with a simplified geometry—i.e., a one-dimensional line heater—and develop the solution in steps.

2.1 One-Dimensional Line Heater

2.1.1 Heater inside the Solid

We begin by considering the temperature field within an infinite circular cylinder with a periodic heat flux at the interior boundary (Carslaw and Jaeger 1959), akin to a *1D heater encased inside an infinite solid* (Figure 2.2).

The governing equation for the steady-state temperature in the cylinder (Φ), assuming no circumferential or axial temperature gradients is

$$\frac{\partial^2 \Phi(r,t)}{\partial r^2} + \frac{1}{r}\frac{\partial \Phi(r,t)}{\partial r} - \frac{1}{\alpha}\frac{\partial \Phi(r,t)}{\partial t} = 0 . \tag{2.15}$$

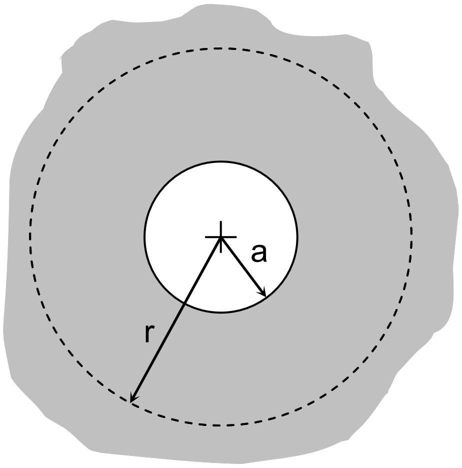

Figure 2.2: Schematic illustration of the cross-section for the geometry for the infinite circular cylinder specimen.

In order to simplify the boundary conditions, the following substitutions are carried out:

$$\Delta\Phi_{AC}(r,t) = \Phi(r,t) - \left(\Phi_0 + \Delta\Phi_{DC}(r)\right), \tag{2.16}$$

$$\Delta\Phi_{DC}(r) = \Phi_{DC}(r) - \Phi_0 , \tag{2.17}$$

where $\mathit{\Delta\Phi}_{AC}(r,t)$ is the steady-state oscillating temperature difference with respect to $\mathit{\Phi}_0 + \mathit{\Delta\Phi}_{DC}(r)$—the ambient temperature $(\mathit{\Phi}_0)$ corrected by the DC temperature rise $(\mathit{\Delta\Phi}_{DC}(r))$. Substituting (2.16) and (2.17) into (2.15) yields

$$\frac{\partial^2 \mathit{\Delta\Phi}_{AC}(r,t)}{\partial r^2} + \frac{1}{r}\frac{\partial \mathit{\Delta\Phi}_{AC}(r,t)}{\partial r} - \frac{1}{\alpha}\frac{\partial \mathit{\Delta\Phi}_{AC}(r,t)}{\partial t} = \frac{d}{dr}\left(r\frac{d\mathit{\Delta\Phi}_{DC}(r)}{dr}\right) = 0\ . \tag{2.18}$$

(2.18) confirms the implicit assumption made in (2.10) that the DC and AC temperature amplitudes are independent of one another. Since the thermal properties of the specimen are extracted from the steady-state temperature oscillations, we will concern ourselves only with solving the left-hand side of equation (2.18). Using separation of variables, we define

$$\mathit{\Delta\Phi}_{AC}(r,t) = \mathit{\Delta T}_{AC}(r)\mathit{\Theta}(t), \tag{2.19}$$

where $\mathit{\Delta T}_{AC}(r)$ is the *spatial evolution* of the temperature oscillations and $\mathit{\Theta}(t)$ gives its *temporal evolution*. From (2.10), we know that the oscillating temperature field will be a harmonic function at twice the excitation frequency; therefore,

$$\mathit{\Theta}(t) = \cos(2\omega t) \equiv \Re(\exp(i2\omega t)). \tag{2.20}$$

Substituting (2.19) and (2.20) into the left-hand side of (2.18) we obtain

$$\Re\left(\frac{d^2 \mathit{\Delta T}_{AC}(r)}{dr^2} + \frac{1}{r}\frac{d\mathit{\Delta T}_{AC}(r)}{dr} - q^2 \mathit{\Delta T}_{AC}(r)\right) = 0\,, \tag{2.21}$$

where q is defined as the wavenumber of the thermal wave given by

$$q = \sqrt{i2\omega/\alpha}\ . \tag{2.22}$$

Equation (2.21) is simply the real part of the modified Bessel equation of order zero whose argument is *qr*. Therefore, the general solution to this equation is given by

$$\mathit{\Delta\Phi}_{AC}(r,t) = \Re\{[c_1 I_0(qr) + c_2 K_0(qr)]\exp(i2\omega t)\}, \tag{2.23}$$

where I_0 and K_0 are the zero-order modified Bessel functions of the first and second kind, respectively. The constants c_1 and c_2 are determined from the boundary conditions: at the inner radius, the *oscillating* heat flux due to the harmonic Joule heating in the heater is given by (2.6) as:

$$@r = a \to 0 \qquad Q = \Re\left(P_{rms}\exp(i2\omega t)\right) = \lim_{a\to 0}\left[-kA_S\frac{\partial \Delta\Phi_{AC}(r,t)}{\partial r}\right]\Bigg|_{r=a}, \tag{2.24}$$

where k is the specimen thermal conductivity and A_S is the surface area of cylinder at the inner radius given by

$$A_S = 2\pi r l_h. \tag{2.25}$$

The second boundary condition requires the temperature oscillations to decay to zero as the radius approaches infinity:

$$@r \to \infty \qquad \Delta\Phi_{AC}(\infty,t) = 0. \tag{2.26}$$

Since the outer radius extends to infinity, we require $c_1 = 0$ for the solution to remain bounded. c_2 is obtained by solving (2.24); therefore, (2.23) reduces to

$$\Delta\Phi_{AC}(r,t) = \Re\left(\frac{p_{rms}}{2\pi k}K_0(qr)\exp(i2\omega t)\right) = \left|\Delta T_{AC}(r)\right|\cos(2\omega t + \phi), \tag{2.27}$$

where p_{rms} is the rms power per unit heater length given by

$$p_{rms} = \frac{I_{h,rms}^2 R_{h,0}}{l_h} = \frac{I_{h,0}^2 R_{h,0}}{2l_h} = \frac{V_{h,0}^2}{2l_h R_{h,0}} \tag{2.28}$$

and

$$\left|\Delta T_{AC}(r)\right| = \frac{p_{rms}}{2\pi k}\left|K_0(qr)\right|. \tag{2.29}$$

Note (2.29) is the same expression originally used in (2.10). Equivalently, the magnitude of the oscillation can be written in rectangular form as

$$\Delta T_{AC}(r) = \frac{p_{rms}}{2\pi k}K_0(qr) = \Delta T_{AC,x}(r) + i\Delta T_{AC,y}(r), \tag{2.30}$$

where

$$\begin{aligned}\Delta T_{AC,x}(r) &= \Re\left(\frac{p_{rms}}{2\pi k}K_0(qr)\right)\\ \Delta T_{AC,y}(r) &= \Im\left(\frac{p_{rms}}{2\pi k}K_0(qr)\right)\end{aligned}.$$

We are not so much interested in determining the *temporal evolution* of the temperature oscillations $(\Delta\Phi_{AC}(r,t))$ as in the *spatial evolution* of the waves which are in-phase $(\Delta T_{AC,x}(r))$ and out-of-phase $(\Delta T_{AC,y}(r))$ with respect to the excitation current as a function of excitation frequency. Therefore, we will restrict the forthcoming discussions to the spatial evolution of the thermal oscillations $(\Delta T_{AC}(r))$, remembering that the temporal evolution can easily be obtained from (2.27).

2.1.2 Heater at the Surface

Now, (2.30) was obtained for a 1D line heater buried within an infinite solid. In our case however, we are dealing with a heater deposited on the *surface* of the specimen. In order to correct our mathematical model, we simply cut the infinite cylinder along a plane perpendicular to the radial direction (Figure 2.3).

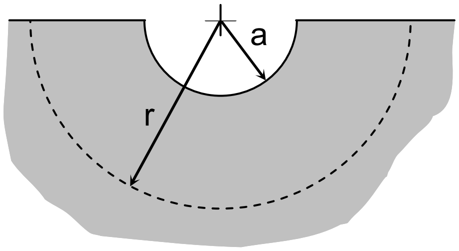

Figure 2.3: Schematic illustration of the cross-section for the geometry for the semi-infinite half-cylinder specimen.

Since the temperature gradients are all in the *radial direction*, this radial cut does not affect the temperature field other than doubling the heat flux from the heater (since the input power is fixed and the surface area is halved). Therefore, (2.30) becomes

$$\Delta T_{AC}(r) = \frac{p_{rms}}{\pi k} K_0(qr). \tag{2.31}$$

Experimentally, this requires *zero heat flux across the specimen surface* (i.e., no conduction, convection or radiation losses to the environment). For this reason, the specimen is placed in a vacuum chamber to minimize conduction and convection heat transfer to the environment. Radiation losses are minimal due to the rapid decay of the temperature oscillations, which in turn minimises the heated area on the surface of the specimen.

In addition, the physical specimen is not a semi-infinite solid, but rather has a finite thickness. Since the thermal waves decay rapidly away from the heat source—following a modified Bessel function of the second kind—we must simply ensure that the penetration depth of the thermal wave is much less than the thickness of the specimen $(\lambda << t_s)$, where the thermal penetration depth is defined as

$$\lambda = \frac{1}{|q|} = \sqrt{\frac{\alpha}{2\omega}} . \tag{2.32}$$

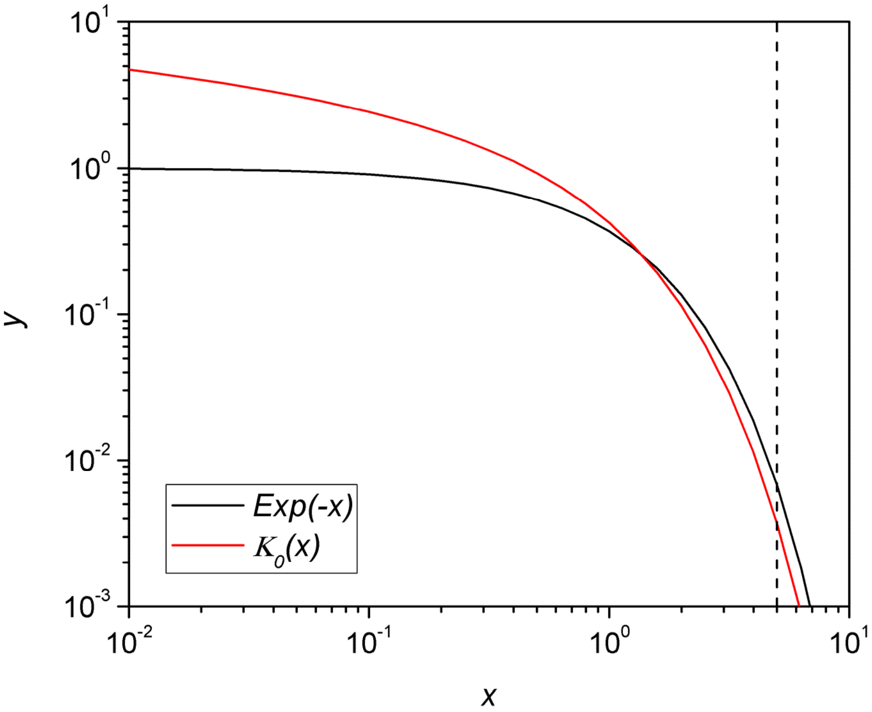

Figure 2.4: Comparison of the decaying amplitudes of the exponential and modified Bessel function of the second kind for a unit length constant. The dotted line indicates five length constants.

Now, given that the physical specimens are not semi-infinite solids and the amplitude of the thermal oscillations decay rapidly away from the heater, it is useful to determine an upper bound on the depth of the heat affected region to ensure the mathematical model is applicable. Since the amplitude of an exponentially decaying function reduces to approximately 1% of its initial magnitude after 5 "length constants", one expects that the magnitude of the thermal oscillations will decrease below 1% of its initial amplitude after 5 thermal penetration depths— as the Bessel function decays faster than an exponential function (Figure 2.4). As such, we state that *the specimen thickness must exceed 5 times the thermal penetration depth to be considered semi-infinite* $\left(t_s > 5\lambda\right)$.

Lastly, the temperature being measured is the heater temperature, which is the same as the specimen surface temperature under the heater, *assuming good thermal contact and small heater height*. As such, let $y = 0$ and $r = x$:

$$\Delta T_{AC}\left(x\right) = \frac{p_{rms}}{\pi k} K_0\left(qx\right). \tag{2.33}$$

Figure 2.5 shows the temporal evolution of the surface temperature oscillations:

$$\Delta \Phi_{AC}\left(qx, \omega t\right) = \Re\left(\frac{p_{rms}}{\pi k} K_0\left(qx\right)\exp\left(i2\omega t\right)\right). \tag{2.34}$$

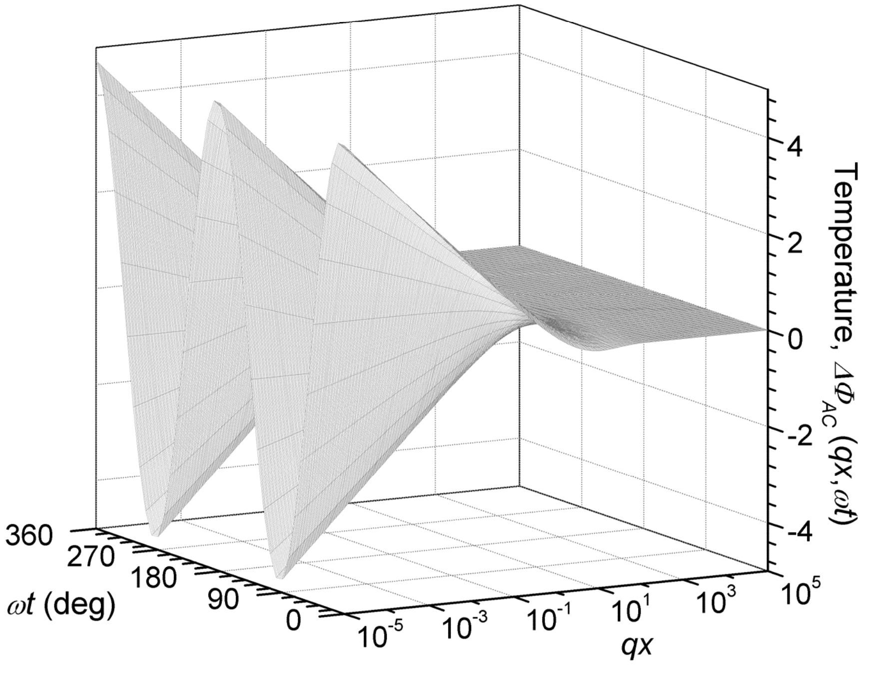

Figure 2.5: 3D surface showing the time evolution of the non-dimensional surface temperature oscillations as a function of distance away from the heater.

2.2 Effects of Finite Width of the Heater

In order to generalise the 1D line solution (i.e., equation (2.33)) to one with a *finite-width*, one needs to superimpose an infinite number of 1D line sources over the width of the heater (Cahill 1990).

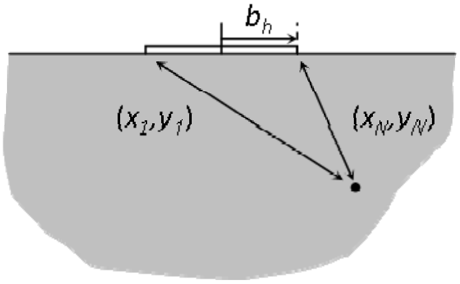

Figure 2.6: Schematic of a finite-width line heater showing the temperature contributions from the extremities of the heater to a point in the specimen.

This leads to a convolution integral, since the temperature at any arbitrary set of coordinates (x, y) within the specimen depends on its relative position to all the line sources (Figure 2.6). A solution to this convolution integral can be easily obtained by performing the following Fourier (wavenumber) transformation:

$$\Psi(\eta) = \frac{1}{2}\int_{-\infty}^{\infty} \psi(x)\exp(-i\eta x)dx, \tag{2.35}$$

$$\psi(x) = \frac{1}{\pi}\int_{-\infty}^{\infty} \Psi(\eta)\exp(i\eta x)d\eta, \tag{2.36}$$

where η is the wavenumber. Since the temperature field is an even function, the Fourier transform pair reduces to the Cosine Fourier transform pair:

$$\Psi(\eta) = \int_{0}^{\infty} \psi(x)\cos(\eta x)dx, \tag{2.37}$$

$$\psi(x) = \frac{2}{\pi}\int_{0}^{\infty} \Psi(\eta)\cos(\eta x)d\eta. \tag{2.38}$$

From (Erdélyi 1954), the Fourier transform of a modified Bessel function of order zero is given as

$$\Delta T_{AC}(\eta) = \frac{p_{rms}}{2k}\left(\frac{1}{\sqrt{\eta^2 + q^2}}\right). \tag{2.39}$$

For a finite heater width, the temperature difference in Fourier space is multiplied by the Fourier transform of a single square wave $(\mathrm{rect}(x))$ from $x = 0$ to b_h:

$$\Delta T_{AC}(\eta) = \frac{p_{rms}}{2k}\frac{1}{\sqrt{\eta^2 + q^2}}\int_0^{b_h}\mathrm{rect}(x)\cos(\eta x)dx = \frac{p_{rms}}{2k}\frac{\sin(\eta b_h)}{\eta b_h\sqrt{\eta^2 + q^2}}. \tag{2.40}$$

Use the inverse Fourier transform (2.38) to convert (2.40) back to real space:

$$\Delta T_{AC}(x) = \frac{1}{\pi}\int_0^{\infty}\Delta T(\eta)\cos(\eta x)d\eta = \frac{p_{rms}}{\pi k}\int_0^{\infty}\frac{\sin(\eta b_h)}{\eta b_h\sqrt{\eta^2 + q^2}}\cos(\eta x)d\eta. \tag{2.41}$$

Since the heater measures the average temperature over the width of the heater, the magnitude of the temperature oscillations measured is average heater temperature:

$$\Delta T_{AC} = \frac{1}{2b_h}\int_{-b_h}^{b_h}\Delta T_{AC}(x)dx = \frac{p_{rms}}{\pi k}\int_0^{\infty}\frac{\sin^2(\eta b_h)}{(\eta b_h)^2\sqrt{\eta^2 + q^2}}d\eta. \tag{2.42}$$

And so, the measured oscillation magnitude for a finite width heater deposited on the surface of the specimen is

$$\Delta T_{AC} = \frac{p_{rms}}{\pi k}\int_0^{\infty}\frac{\sin^2(\eta b_h)}{(\eta b_h)^2\sqrt{\eta^2 + q(\omega)^2}}d\eta = \Delta T_{AC,x} + i\Delta T_{AC,y}. \tag{2.43}$$

There is no closed-form solution to the above integral; rather, asymptotic solutions can be obtained in the limit of small and large thermal penetration depths.

2.3 *Approximate Solutions to the Exact Equation*

Equation (2.43) for the magnitude of temperature oscillations for a heater with finite width was solved numerically using an adaptive Simpson quadrature algorithm in Matlab® (Figure 2.7). The numerical integration was carried out over the interval $\left[10^{-10}, 10^{10}\right]$. Increasing the limits of wavenumber changed the temperature amplitude by less than 1%.

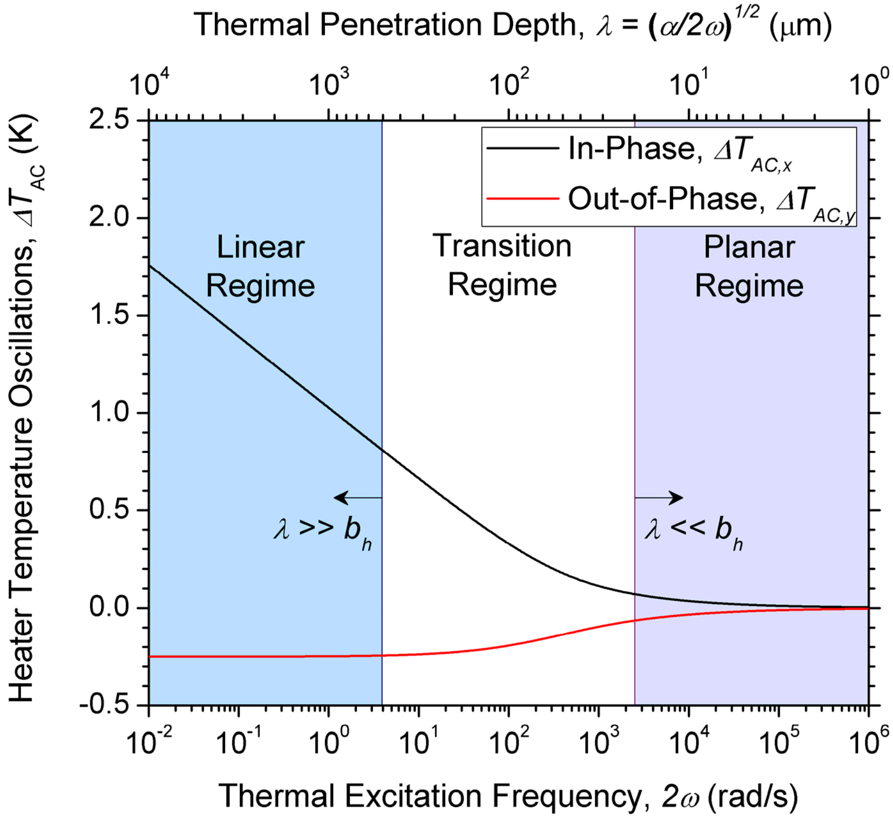

Figure 2.7: In-phase (black line) and out-of-phase (red line) components of the temperature oscillations vs. thermal excitation frequency (2ω) and thermal penetration depth (λ). The rms power per unit length (p_{rms}) is 1 W/m, the heater half-width (b_h) is 10 μm, the thermal conductivity (k) is 1 W/m·K and the thermal diffusivity (α) is 1 mm^2/s. The linear regime (light blue shade region) is used to determine the thermal conductivity of the specimen.

Figure 2.7 shows the real (in-phase) and imaginary (out-of-phase) components of the temperature oscillations as a function of thermal excitation frequency (2ω) and thermal penetration depth (λ). One can see two distinct regimes in the behaviour of the temperature oscillations. For “large” thermal penetration depths, the in-phase temperature decays logarithmically—linearly in a semilog plot—and we call this frequency range the *linear regime* (light blue shaded region). The linear regime is also characterised by a constant negative out-of-phase temperature leading to zero phase lag in the limit of zero frequency. For “small” thermal penetration depths, the in-phase and out-of-phase temperature magnitudes are equal, but opposite in sign—leading to a 45° phase lag between the temperature and current—and the in-phase magnitude decays more slowly than in the linear regime. This is the so-called *planar regime* (violet shaded region). Between these two extremes, there is a *transition regime* (un-shaded region).

Using such qualifiers as “large” and “small” for the thermal penetration depth requires an appropriate length scale with which to compare. The only other length scale in the heat equation is the half-width of the heater (b_h). Therefore, the linear regime is defined as the domain in which the thermal penetration depth is “much larger” than the heater half-width, and conversely for the planar regime.

Furthermore, by taking the limit of small and large heater half-width, one can obtain closed form solutions for each regime. First consider the planar regime, for which the heater half-width is much larger than the thermal penetration depth $(b_h >> \lambda)$, such that

$$\lim_{b_h \to \infty} \frac{1}{\pi b_h} \left[\frac{\sin(b_h \eta)}{\sin(\eta)} \right]^2 = \delta(\eta). \tag{2.44}$$

Substitute (2.44) into (2.43) to obtain

$$\Delta T_{AC} = \frac{p_{rms}}{b_h k} \int_0^\infty \frac{\sin^2(\eta)\delta(\eta)}{(\eta)^2 \sqrt{\eta^2 + q(\omega)^2}} d\eta \approx \frac{\tilde{p}_{rms}}{kq}, \tag{2.45}$$

where $\tilde{p}_{rms}$ is the rms power per unit heater *area* given by

$$\tilde{p}_{rms} = \frac{p_{rms}}{2b_h} = \frac{P_{rms}}{2b_h l_h} = \frac{V_0^2}{4b_h l_h R_0}. \tag{2.46}$$

Equivalently, (2.45) can be written as

$$\Delta T_{AC}(2\omega) \approx \frac{\tilde{p}_{rms}}{e\sqrt{2\omega}} \exp(-i\pi/4), \tag{2.47}$$

where e is the specimen thermal effusivity defined as

$$e = \sqrt{kC_p}.$$

The constant phase shift of -45° in (2.47) is consistent with the equal magnitude temperature components in the planar regime in Figure 2.7. Equation (2.47) is approximately equal to the solution for one-dimensional heat conduction in a semi-infinite solid with a harmonic heat flux at the surface (Carslaw and Jaeger 1959).

Conversely in the linear regime, the heater half-width is much smaller than the thermal penetration depth $(b_h << \lambda)$, such that

$$\lim_{b_h \to 0} \frac{\sin(b_h \eta)}{(b_h \eta)} = 1. \tag{2.48}$$

In addition, since large wavenumber oscillations have relatively negligible amplitude and decay quickly, the integral is dominated by wavenumbers between $1/\lambda < \eta < 1/b_h$. Substituting (2.48) into (2.43) and setting the upper integration bound to $1/b_h$ we obtain

$$\Delta T_{AC} = \frac{p_{rms}}{\pi k} \int_0^{1/b_h} \frac{1}{\sqrt{\eta^2 + q^2}} d\eta \approx -\frac{p_{rms}}{\pi k} \left(\ln(q b_h) - \xi \right), \tag{2.49}$$

where ξ is a fitting constant having a value of roughly 0.922. Re-writing (2.49) in terms of thermal excitation frequency, one obtains

$$\Delta T_{AC}(2\omega) = -\frac{p_{rms}}{2\pi k} \left(\ln(2\omega) + \ln\left(b_h^2/\alpha\right) - 2\xi \right) - i \frac{p_{rms}}{4k}. \tag{2.50}$$

(2.50) can also be written in terms of measurable quantities, such as voltages and resistances using (2.12) and (2.28)

$$V_{h,3\omega}(2\omega) = -\frac{V_{h,0}^3 \beta_h}{4\pi l_h k R_{h,0}} \left(\ln(2\omega) + \ln\left(b_h^2/\alpha\right) - 2\xi \right) - i \frac{V_{h,0}^3 \beta_h}{8 l_h k R_{h,0}}. \tag{2.51}$$

As predicted in Figure 2.7, the in-phase temperature decays logarithmically with respect to the thermal excitation frequency (2ω), and the out-of-phase component is constant.

Now that approximate analytical solutions for the linear and planar regimes have been found, they can be compared to the exact numerical solution in order to quantify appropriate boundaries of applicability for these approximations in terms of ratios of thermal penetration depth to heater half-width (Figure 2.8).

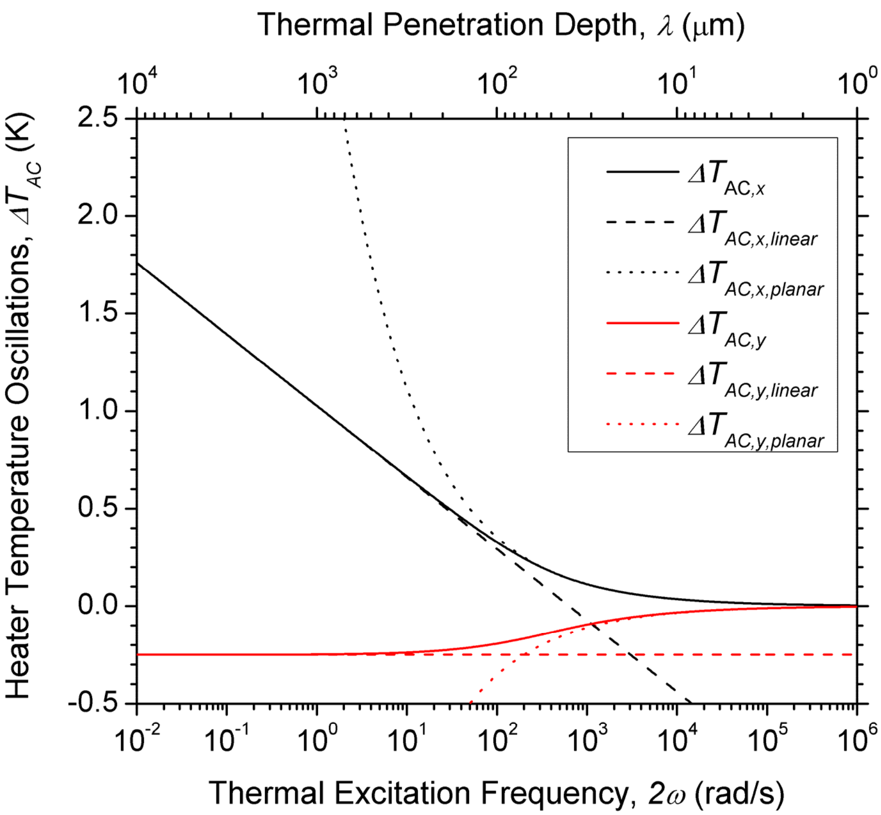

Figure 2.8: Comparison of the exact solution (solid lines) with approximations for the linear (dashed lines) and planar regimes (dotted lines) for the temperature oscillations of the heater. The in-phase component is coloured black while the out-of-phase signal is red. The parameters (i.e., p_{rms}, b_h, k and α) are the same as in Figure 2.7.

The precise boundaries for the different regimes are somewhat arbitrary and depend on our acceptable level of error in the results (Figure 2.9). By convention, the boundary on the linear regime is set as $\lambda > 5b_h$, yielding a maximum rms error of 0.25%. Similarly, for the boundary for the planar regime is $\lambda > b_h/5$ for a discrepancy of 0.15%. However, given that the specimens have finite thickness, the boundaries of the linear regime become

$$t_s/5 > \lambda > 5b_h. \tag{2.52}$$

Equation (2.52) is useful in the design of experiments because it provides an estimate of the minimum specimen thickness required for a given heater width in order to obtain a linear regime:

$$t_s > 25b_h. \tag{2.53}$$

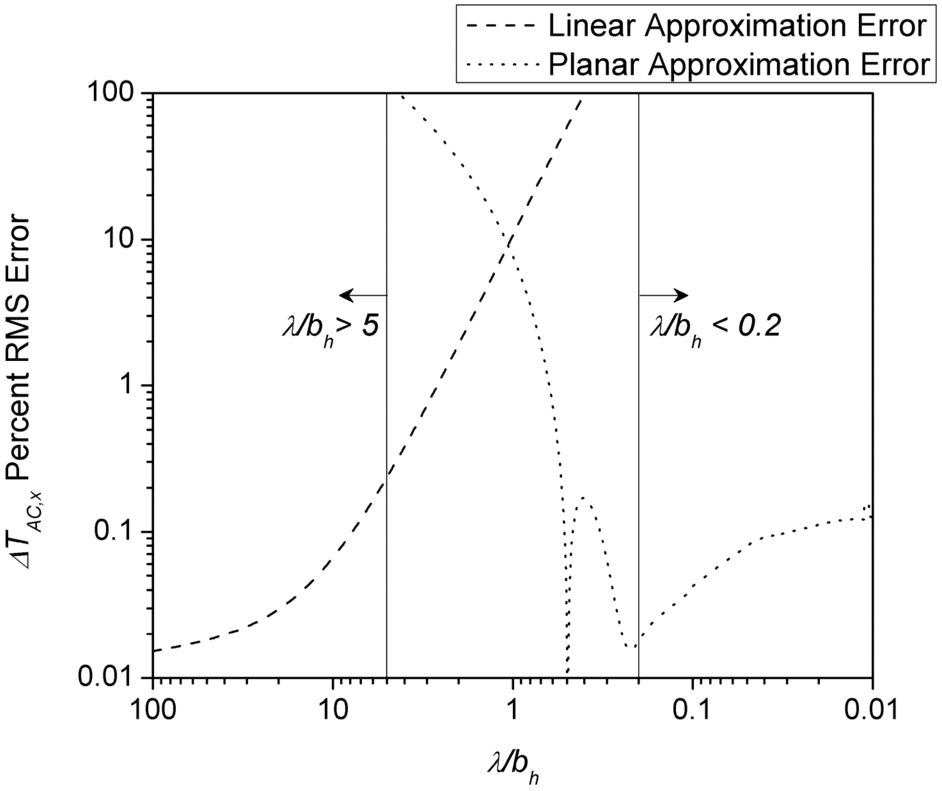

Figure 2.9: In-phase temperature magnitude %rms error vs. the ratio of thermal penetration depth to heater half-width (λ/b_h). Both the discrepancy between the exact solution and the linear approximation (dashed line) and that of the planar approximation (dotted line) are given shown. The conventional cut-off points are indicated by the solid lines. The parameters (i.e., p_{rms}, b_h, k and α) are the same as in Figure 2.7.

2.4 Conclusion

Equation (2.51) is extremely powerful: it indicates that the thermal conductivity can be obtained directly—without any fitting parameters—from either the slope of the in-phase magnitude or the magnitude of the out-of-phase temperature oscillations. This is rare for transient thermal measurement techniques: normally independent measurements of the thermal diffusivity and volumetric heat capacity are required to obtain the thermal conductivity.

The most important aspect of any 3ω measurement apparatus is a precise measurement of the minute third harmonic signal across the specimen heater. As such, effort has been expended to identify and eliminate any spurious signals at 3ω. However, one must also ensure that the output from the heater itself is an accurate indicator of the temperature fluctuations in the specimen. Above, we assumed negligible thermal resistance between the heater and the specimen. This crucial assumption rests on our ability to *fabricate heaters which are in intimate thermal contact with the specimen surface*. In the next chapter, we will address these issues by examining the heater fabrication process as well as the electrical interface between it and the 3ω apparatus.

Chapter 3: Specimen Preparation

In Chapter 2, we found that the heater/RTD required a *large* temperature coefficient of resistance (TCR) in order to generate a measurable resistance change as a function of temperature. In general, platinum is the material of choice for RTDs, due to the linearity of its TCR over a wide range of temperatures and its stability at high temperatures. However, since the amplitude of the temperature oscillations is small, platinum is not required. Instead, Gold was chosen for its large TCR and lower cost. Unfortunately, both Gold and platinum do not adhere well to ceramic substrates; therefore a 10 nm Chrome "adhesion" layer was first deposited on the substrate to increase adhesion of the heater (Huang et al. 2003).

This section will describe the different methods used in this work to deposit the Gold/Chrome thin film heaters. The process involves 3 major steps:

- surface cleaning;
- deposition, and;
- patterning.

3.1 Surface Cleaning

In order to minimize thermal interface resistance and ensure adhesion of the metal film to the specimen, a clean surface free of particulate matter and solvents is required. This was accomplished with a simple 4 step process.

The specimen was immersed in an acetone bath and sonicated at 40°C for 10 minutes to remove the surface contaminants. Since acetone leaves its own residue, it must be removed by a similar treatment using isopropyl alcohol followed by deionised water. Finally, the specimen is blown dry with compressed nitrogen, to prevent any residues in suspension from re-depositing on the surface.

For water-soluble or extremely brittle specimens, a dry cleaning process, such as a plasma asher can be used to remove impurities and trace solvents from the surface of the specimen. The process uses energetic plasma derived from argon or oxygen gas.

3.2 Heater Deposition

Deposition techniques generally fall in two different categories: *physical vapour deposition* (PVD) and *chemical vapour deposition* (CVD). CVD techniques grow thin films on the substrate via *chemical reactions* of precursor compounds. For example, silane gas (SiH_4) is used as a precursor for silicon deposition. These reactions take place in a controlled environment above the substrate and the products precipitate to form a coating.

Conversely, PVD creates coatings by *physically* removing atoms from a piece of the desired material (the target) and transporting the ejected material to the specimen (the substrate). This can be accomplished by heating the target above its boiling point (evaporation) or bombarding it with energetic ions (sputtering).

Few CVD techniques have been developed for depositing metals since it is much easier and more cost-effective to use PVD. As such, we will concentrate our attention to physical vapour deposition techniques. The choice of deposition technique affects the geometry, kinetics, chemistry and microstructure of the thin film and can impact subsequent processing steps.

3.2.1 Evaporation

As the name implies, evaporation deposition seeks to create thin films by evaporating the target material onto the substrate. The target is placed inside an evacuated chamber and the evaporated atoms condense onto the substrate. Thin films created using evaporation tend to be *non-conformal*, meaning that the coverage is line-of-sight only. Non-conformal coatings are used with patterning techniques such as lift-off and shadowmask patterning (see below).

The evaporator used in this work was a BOC Edwards Auto 306 electron-gun deposition system. The base pressure of the chamber prior to deposition was below 1 µTorr. Typical deposition rates were 0.2 nm/s and 0.5 nm/s for chrome and gold, respectively.

3.2.2 Sputtering

For sputtering, the material is released from the target by bombarding it with plasma. As such, processing temperatures are much lower than in evaporation. The ejected material reaches the substrate via diffusive transport through the plasma, thus yielding a *conformal* coating. As such, sputtering is normally used in conjunction with etching techniques (see below). The adhesion of sputtered films tends to be better than evaporated coatings. Due to the physical nature of the ejection process, a wide range of materials can be sputter deposited.

Using the Denton Explorer 14 sputter deposition instrument at McGill University's Nanotools Microfab laboratory, chrome/gold thin films were deposited onto the substrates. Applying a direct current of 0.2 A onto the gold target under an argon atmosphere at 8 mTorr yielded a deposition rate of 0.35 nm/s. Similarly for the chrome deposition, a sputter rate of 0.2 nm/s was achieved at 0.6 A and 8 mTorr of argon.

3.3 Patterning

Functional elements of microsystems are created by patterning and etching thin films deposited onto the substrate. Photolithography is the usual method used to pattern features for microelectronics and microsystems. However, there are a growing number of applications, principally microsystems, which do not require the full resolution of photolithography. For these applications, simpler low-cost approaches such as soft lithography (stamping) and shadowmask deposition can be used for patterning.

3.3.1 Photolithography

Photolithography—writing with light—creates patterns in a UV-sensitive material (called photoresist), which serves as an etch mask for a subsequent etching process (Figure 3.1). First, a drop of photoresist is placed at the center of the substrate and spin coated on the substrate. Second, a positive photomask, containing the features one wishes to transfer to the photoresist, is placed above the substrate. By exposing the substrate to UV radiation, the exposed portion of the photoresist will become soluble. The photoresist is then developed, leaving behind the desired pattern of unexposed resist. The patterned photoresist can be used in two different ways to achieve the final with the desired material: etching or lift-off.

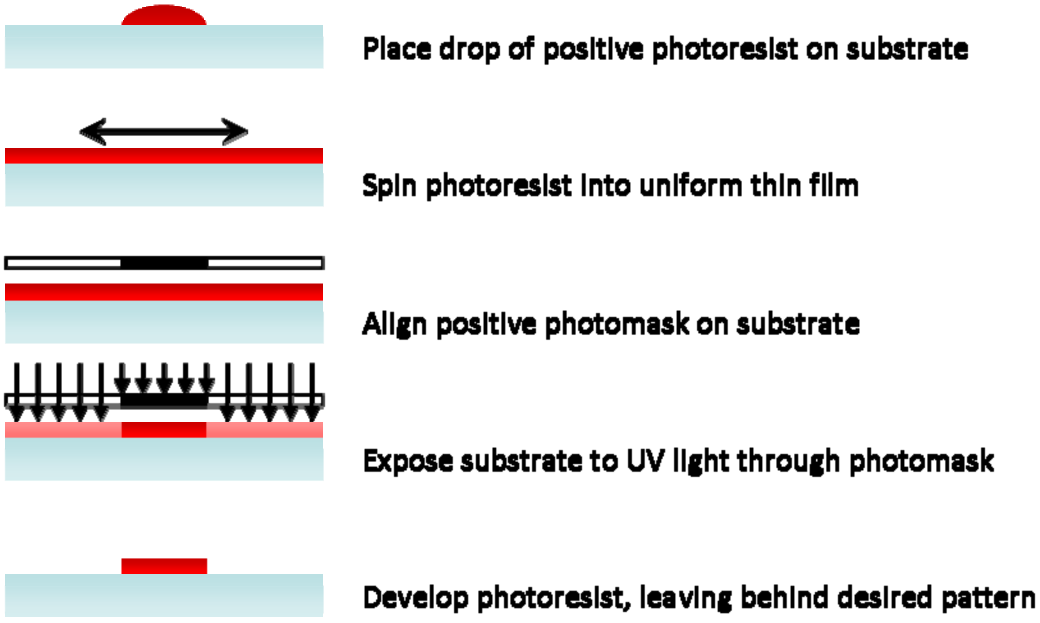

Figure 3.1: Basic photolithography process flow using positive photoresist and mask. The sky blue rectangle represents the substrate and the red material symbolizes the photoresist film. Note: dimensions not to scale.

3.3.1.a Etching

If etching is used, then a uniform thin film is deposited on the substrate prior to photolithography (Figure 3.2). Then, the developed photoresist serves as an etch mask for the subsequent etch process. Following the etching process, the resist is stripped off the substrate resulting in the desired pattern in the deposited thin film. In the case of etching metals, such as Gold and Chrome, the etchants are concentrated acids. Non-withstanding the safety precautions needed to handle concentrated acidic solutions, the main difficulty with wet etch processes is the precision required to transfer the photoresist pattern to the metal with high fidelity. Wet etching operates on the basis of differential selectivity, that is, the etchant will etch through the metal faster than through the photoresist or substrate, therefore precise timing is important to obtain the desired pattern. It was rather difficult to produce thin lines of uniform width using this technique (Figure 3.3). In fact, most of the lines made contained complete breaks, rendering them useless.

Figure 3.2: Wet etching schematic process flow. The sky blue rectangle represents the substrate, while the yellow and red materials symbolize the deposited film and photoresist, respectively. Note: dimensions not to scale.

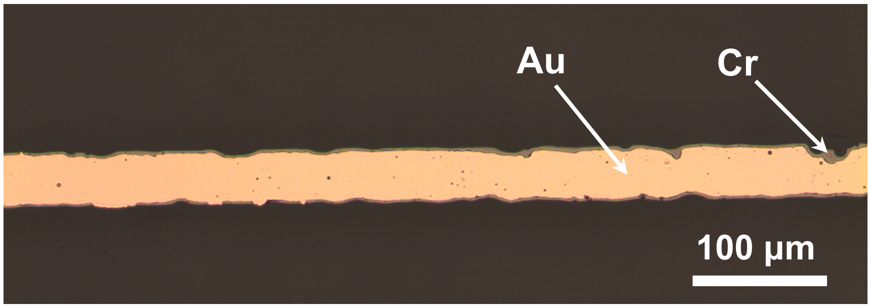

Figure 3.3: Optical micrograph of a wet-etched Gold film (orange region) overtop a Chrome adhesion layer (grey region). The Chrome layer measured 10 nm in thickness while the Gold thin film was 200 nm thick. Since the two layers were etched independently using a timed etch stop, it was difficult to obtain lines of uniform width.

3.3.1.b Lift-Off

On the other hand, the lift-off technique functions in the opposite way to the etching process: rather than deposit the thin film prior to photolithography, the metal is deposited afterward (Figure 3.4). Instead of using a positive photomask, lift-off makes use of a negative mask. Also, the intensity of the UV radiation is increased in order to undercut the sidewalls in the resist mask to facilitate the lift-off process. When the photoresist is dissolved, the metal above it is removed as well, leaving behind the patterned metal film. This process was never implemented, due to the lack of an evaporator at McGill University. Instead, we decided to go directly for shadowmask deposition, removing the need to purchase a negative photomask.

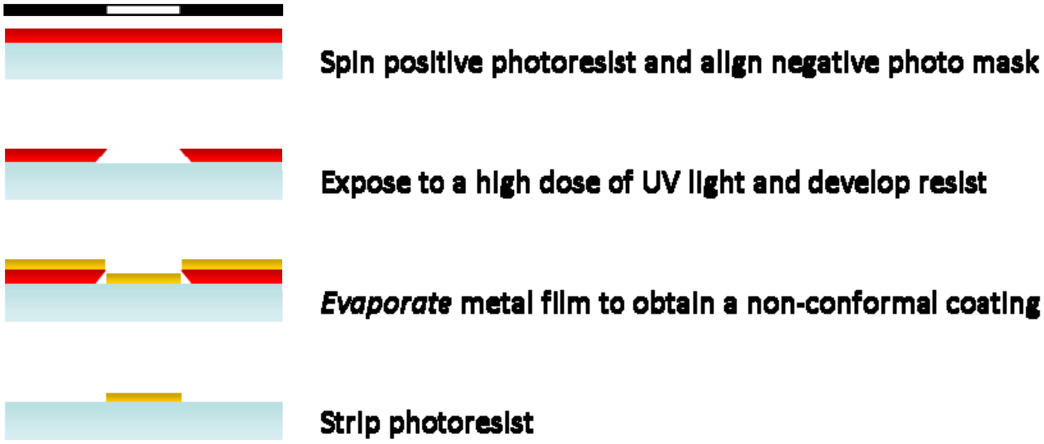

Figure 3.4: Lift-off process flow. The sky blue rectangle represents the substrate, while the yellow and red materials symbolize the deposited film and photoresist, respectively. Note: dimensions not to scale.

3.3.2 Shadowmask

As an alternative to photolithography, shadowmask deposition is essentially "micro-stencilling", using evaporated metal films rather than paint (Figure 3.5). It is very similar to lift-off, however you by-pass the expensive photolithography step while sacrificing feature size resolution. Given that our smallest feature size (the line width) is relatively large by photolithography standards, we opted to forgo lift-off and attempt shadowmask deposition directly. One takes a thin steel foil (i.e., shadowmask) and laser cuts the desired pattern into it. The foil is then clamped onto the surface of the substrate and placed in the evaporator. The chrome and Gold films are subsequently deposited through the holes in the shadowmask. The mask is removed leaving behind a faithful negative reproduction of the patterned shadowmask. Due to the non-conformality of evaporation, the edges of the patterned metal films are nearly identical to those on the mask (Figure 3.6). In fact, any debris in the shadowmask opening was faithfully transferred onto the heater (Figure 3.7). The shape and spacing of the gaps and holes on different specimens were constant and unique for a given mask; such that the mask used to create the heater could be identified based on a micrograph of the line. Therefore, the "bad" shadowmasks with gaps or holes could be identified and discarded. This method was extremely successful in creating uniform lines with widths of 40 microns or larger. The minimum feature sizes were limited by our ability to create steel shadowmasks with smaller features.

Any impurities in the Gold heater would dramatically lower its temperature coefficient of resistance (Pollock 1982). Therefore, the binary films could not be annealed after the deposition in order to prevent diffusion of chrome atoms into the Gold layer (Huang et al. 2003). It is assumed that the diffusion during the 3ω measurements themselves is negligible since the maximum DC temperature increase was less than 15 K and the amplitude of the temperature oscillations was roughly 1 K.

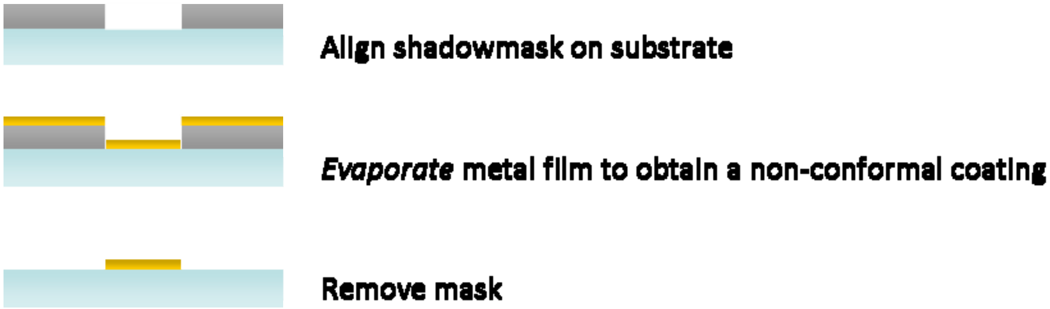

Figure 3.5: Shadowmask deposition process flow. The sky blue rectangle represents the substrate, while the yellow and grey materials symbolize the deposited film and steel shadowmask, respectively. Note: dimensions not to scale.

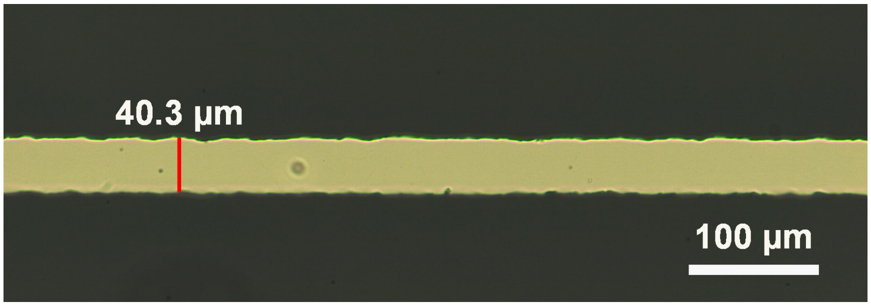

Figure 3.6: Optical micrograph of a shadowmask deposited heater on a fused quartz specimen. The heater was created with shadowmask "A" giving a uniform line, free of holes or gaps.

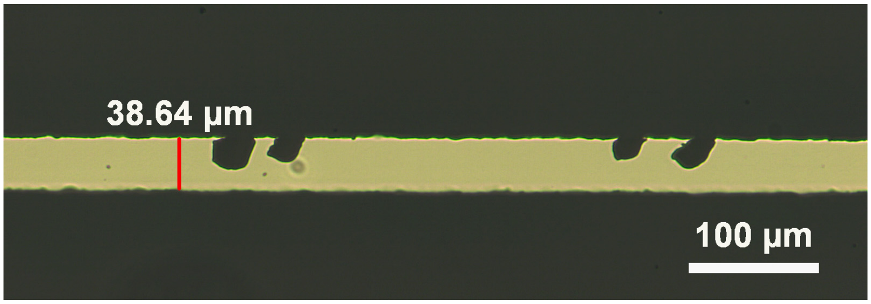

Figure 3.7: Optical micrograph of a shadowmask deposited heater on a fused quartz specimen. The heater was created with Shadowmask "C" yielding poor uniformity.

3.4 Electrical Interface

In order to interface the metal heater to the measurement circuit, contact pads were patterned at both ends of the heater. Contact pads are used in microelectronics and microsystems to bridge the length-scale gap between on-chip microscale interconnects and macro-sized PC board components. There are three different ways of connecting on-chip elements with electronics circuits: wire-bonding, micro-probes and spring-loaded "pogo pins".

3.4.1 Wire-Bonding

Packaging and wire-bonding is the most widely used method for interfacing microfabricated elements with electronic circuits. It is used where permanent connections are wanted.

A package is a plastic receptacle surrounded by a number of contact pads (thin metal pads, usually made of Gold or Aluminium) linked to metal pins. The chip is bonded to the receptacle and thin wires are bonded between the contact pads on the chip and the package.

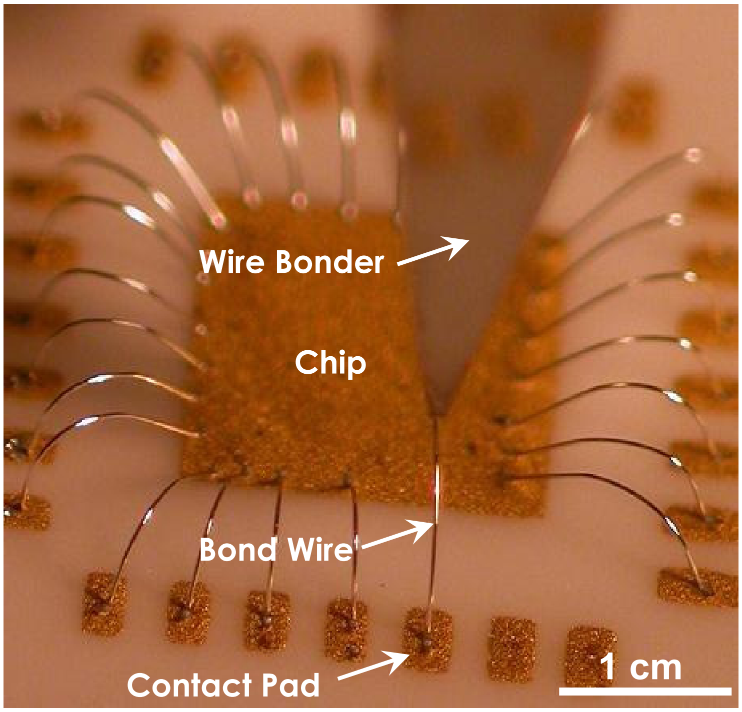

Figure 8: Optical micrograph of a wire bonder testing substrate (ProtoConnect 2006).

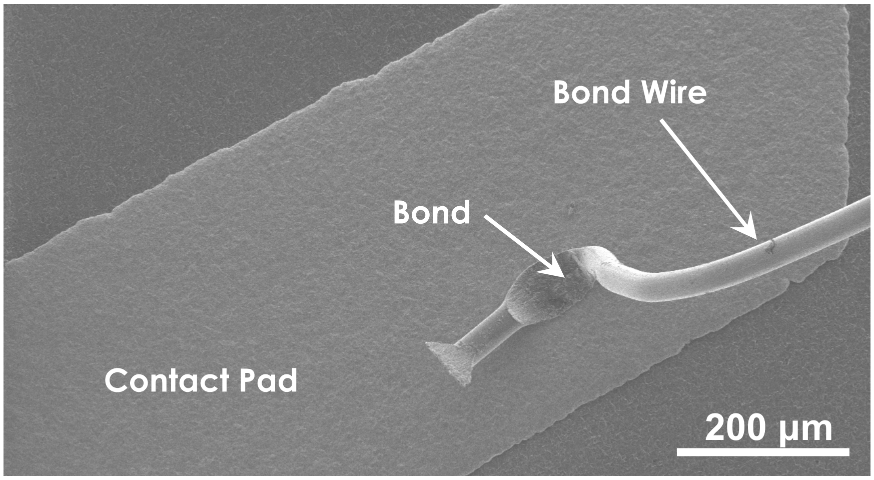

Figure 3.9: Scanning electron micrograph of a wire bond. Shown in this picture is the package-end of the bond wire.

Placing the package into a socket soldered onto a PC board completes the process and the chip is now connected to the rest of the circuit.

This method is great when many electrical connections need to be made in a tight space. Unfortunately, due to the ever shrinking size of electronics, the largest packages readily available can only accommodate a 1.5 cm^2 substrate, thus limiting the length of the heater.

3.4.2 Micro-Probes

Micro-probes are commonly used in the electronics industry for device testing at the prototyping level. It enables easy temporary on-chip electrical connections electrical test equipment. Micro-probes are simply small metal pins mounted on the end of metal rod (the probe holder) (Figure 3.10). Precise placement of the micro-probes onto the small contact pads (generally on the order of 100 μm) is done using 3-axis positioners with micrometer-level precision under a microscope. Although micro-probes become burdensome when a large number of connections need to be made, they are a great alternative to wire-bonding when a few temporary contacts are needed for device testing. Unfortunately, using microprobes within a vacuum environment requires a custom-made vacuum chamber to accommodate the feedthroughs for the 3-axis positioners.

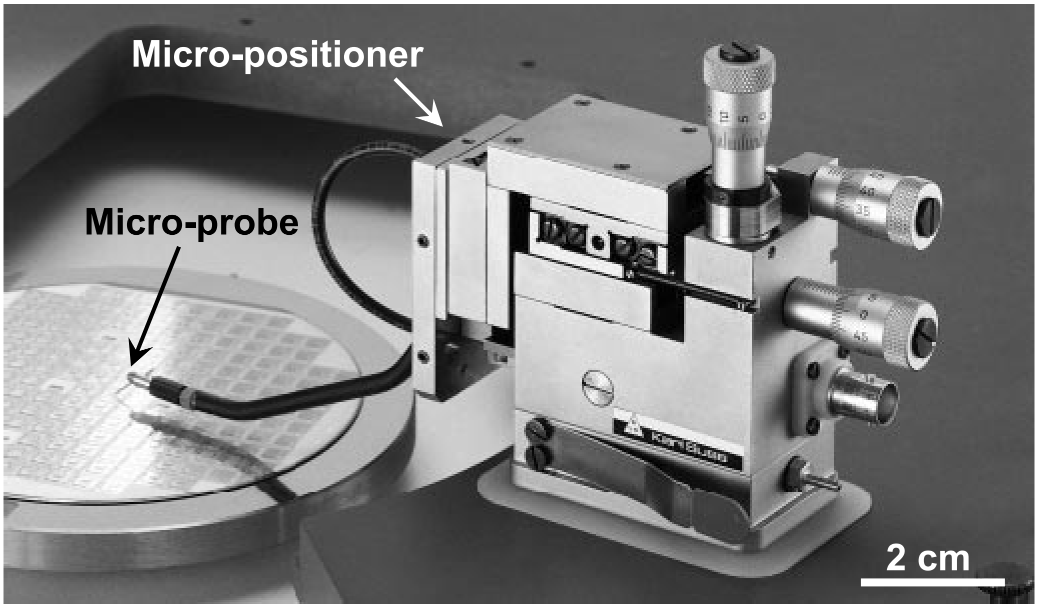

Figure 3.10: Micro-probes used for wafer testing (Karl_Suss 2007).

3.4.3 Pogo Pins

The last alternative is another common device testing interface used in the electronics industry at the manufacturing level. They are also commonly used when reliable temporary electrical connections are needed, such as battery packs for portable electronic devices. As the name implies, pogo pins are linear spring-loaded pins that are pressed onto the on-chip contact pads. They are mounted directly on a PC board (so-called surface mount) or press-fit into a plastic fixture with a lead wire soldered to the end of the pin (through-hole).

Figure 3.11: 6-point push pogo pin (Solarbotics 2008).

The pogo pins are a great low cost alternative to micro-probes for a fixed probing geometry. They also have the advantage of requiring a very small footprint, which is advantageous within the confines of a vacuum chamber. For these reasons I have chosen to use pogo pins.

3.5 Specimen Mount

In order to use through-hole pogo pins (6-point push pogo pin by Solarbotics (Figure 3.11)), a custom-made mounting system was designed and built in-house (Figure 3.12). The system consists of a large Aluminium base, guide pins and a Delrin® cross-beam. The base provided stability and rigidity to the system as well as a large thermal reservoir to maintain a constant specimen temperature. Two Aluminium rods were press-fit into the base to act as vertical guide pins for the mount. The sleeves of the pogo pins were press-fit into the Delrin® cross-beam. The electrical connection is made by placing the specimen on the base and sliding the cross-beam down on along guide pins until the measured electrical resistance across the specimen has stabilized (~90% of the pogo pin travel).

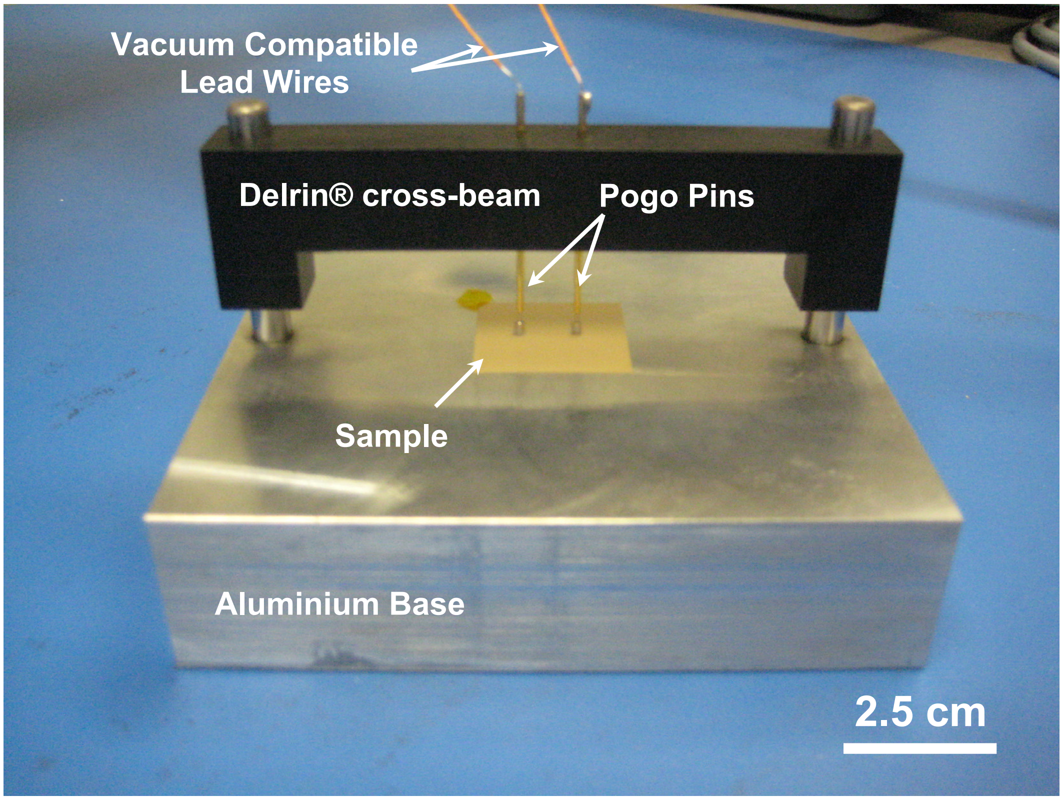

Figure 3.12: Photograph of the pogo pin mount.

The cross-beam maintains the pressure of the spring-loaded pins due to static friction between the plastic cross-beam and the metal guide pins. Contact resistance is minimized by coating the ends of the pins with silver paint (High purity silver paint by SPI). Vacuum compatible wires (30 AWG Single strand, Kapton® insulation by Insulator Seal) were soldered onto the ends of the pogo pin sleeves. The other end is connected to the vacuum-side of BNC electrical feedthroughs (Grounded shield, 2-pin BNC feedthrough by Insulator Seal) via push-on pins (Figure 3.13). A ball of solder (1a) is applied to the exposed end of the vacuum wire (1) and fastened into the push-on pin (2) by tightening a clamping screw (2a). The push-on pin is pressed onto the vacuum-side feedthrough pin (3) which is coupled to an air-side BNC connector (4). The flange (5) is attached to a vacuum chamber port (Figure 3.14) and the vacuum seal is maintained by an elastomer O-ring (6).

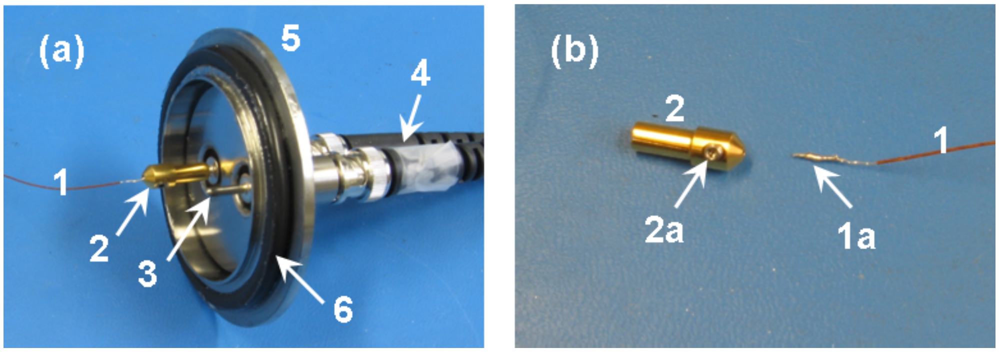

Figure 3.13: Photograph of the electrical feedthrough assembly (a) and a close up of the push-on pin (b). See the text for a description of each element.

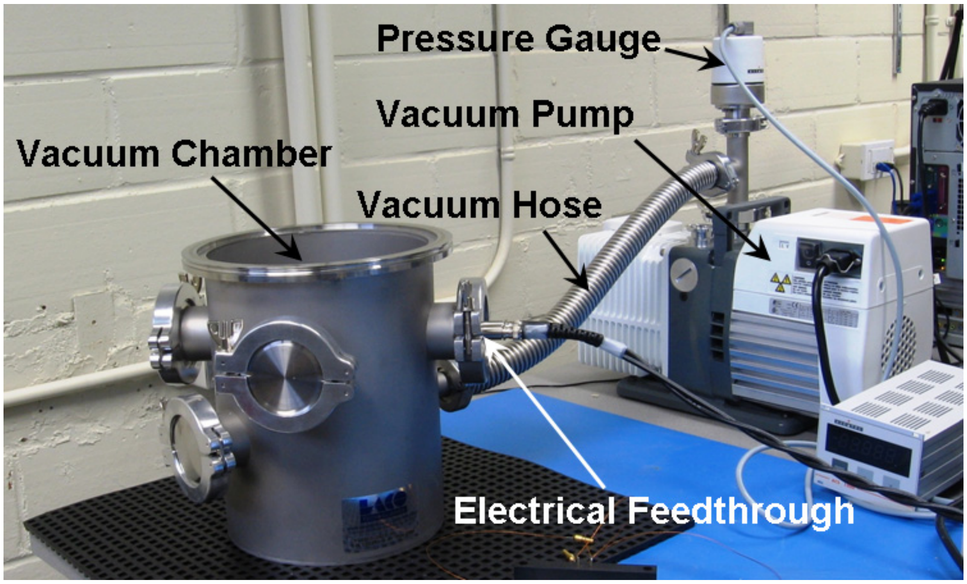

Figure 3.14: Photograph showing the vacuum chamber and rotary vane vacuum pump.

3.6 Conclusions

The most important concern with respect to specimen preparation is repeatability: effort has been expanded to ensure that the specimen heaters are constructed in a controlled and uniform manner. For this reason we chose the shadowmask deposition technique, as it yielded the most consistent results, at the expense of larger line widths. This limits the minimum thickness of the specimens that can be analysed.

In the next section, we will describe the experimental apparatus used to implement the 3ω technique.

Chapter 4: Implementation of the 3ω Technique

In order to implement the 3ω technique, a low noise, low distortion AC signal is created by a function generator and fed through the microfabricated metal film deposited on the specimen surface (Figure 4.1). The metal film behaves both as a resistive heater and resistance thermometer detector (RTD). The heater is connected to Wheatstone bridge in order to detect the weak 3ω voltage. Lastly, the output from the bridge is measured using a lock-in amplifier. The whole system is controlled by a personal computer using a custom LabVIEW virtual instrument.

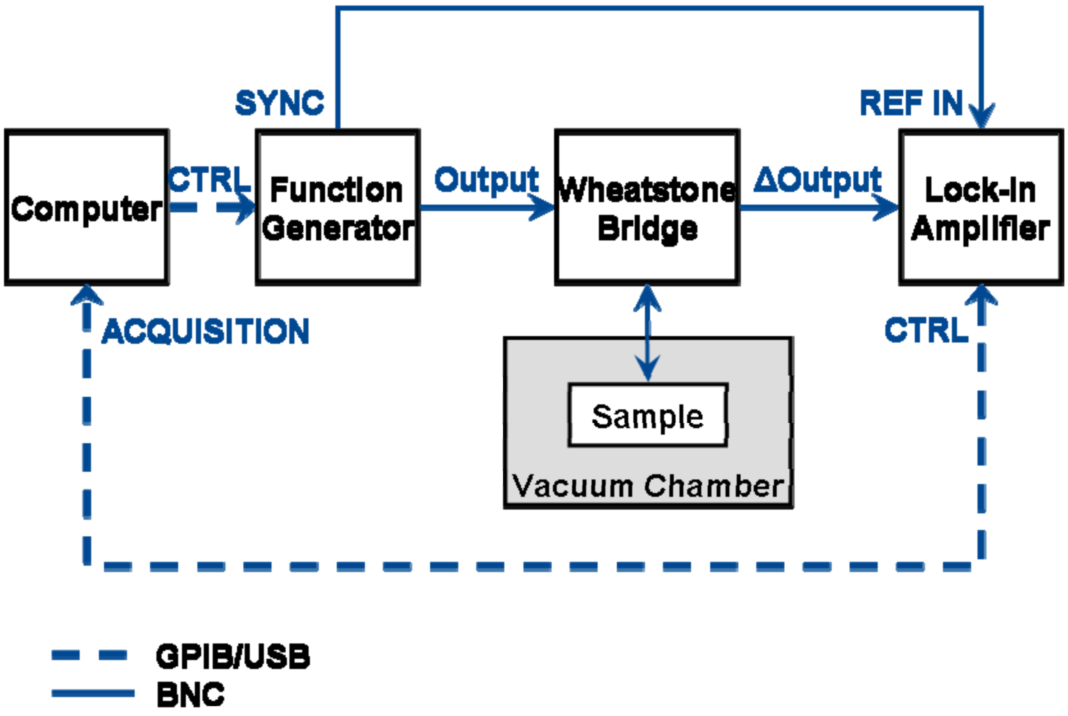

Figure 4.1: Schematic diagram of the 3ω apparatus.

The main objective in the design of the 3ω apparatus is to precisely and accurately measure the in-phase and out-of-phase components of the 3ω voltage. This requires attenuation of any stray third harmonic signals. The largest sources of spurious 3ω voltages were identified as the harmonic noise of the function generator and the Joule heating within the other resistive elements of the Wheatstone bridge (Moon et al. 1996).

4.1 Function Generator

Any function generator used to create a sinusoidal voltage signal will invariably generate noise. Of special concern to us is the harmonic distortion created by the function generator, particularly the noise at the 3rd harmonic. If not properly controlled, harmonic distortion can be a major source of error in the experimental results.

The sinewave is generated using a direct digital synthesis function generator (Agilent 33220A), which converts values from a stored look-up table to an analog signal using a digital-to-analog converter (DAC). Harmonic distortion is generated due to integral (overall) nonlinearities in the DAC transfer function—which relates the input and output of a linear time-invariant function (Figure 4.2). For example, the transfer function for an ideal resistor—with zero temperature coefficient of resistance (TCR)—is a straight line: the current (input) is linearly proportional to the voltage (output); however, for a real resistor, the resistance will increase for larger inputs, generating larger relative voltages. Therefore, the 3ω voltage due to Joule heating can be understood as being the result of a non-linearity in the resistive element's transfer function.

Total harmonic distortion (THD) is a parameter used to quantify the importance of the harmonic noise electronic equipment. It is defined as

$$\mathrm{THD} = \frac{\sum_{n=1}^{5} V_{n\omega}^2}{V_{\omega}^2}, \tag{3.1}$$

where V_{ω} is the peak voltage amplitude of the fundamental signal and the $V_{n\omega}$ is the peak voltage amplitude of the n^{th} harmonic (Wilson et al. 2004). Only the first five harmonics are used to calculate the THD since the amplitude of the higher harmonics decays rapidly with increasing harmonic number. In our case, the THD of the function generator is quoted as 0.04% of the output signal, or 2500 times smaller than the fundamental signal, which is on the same order of magnitude as the 3ω voltage. Therefore, additional measures must be taken to remove these spurious signals. This is accomplished using common-mode cancellation techniques.

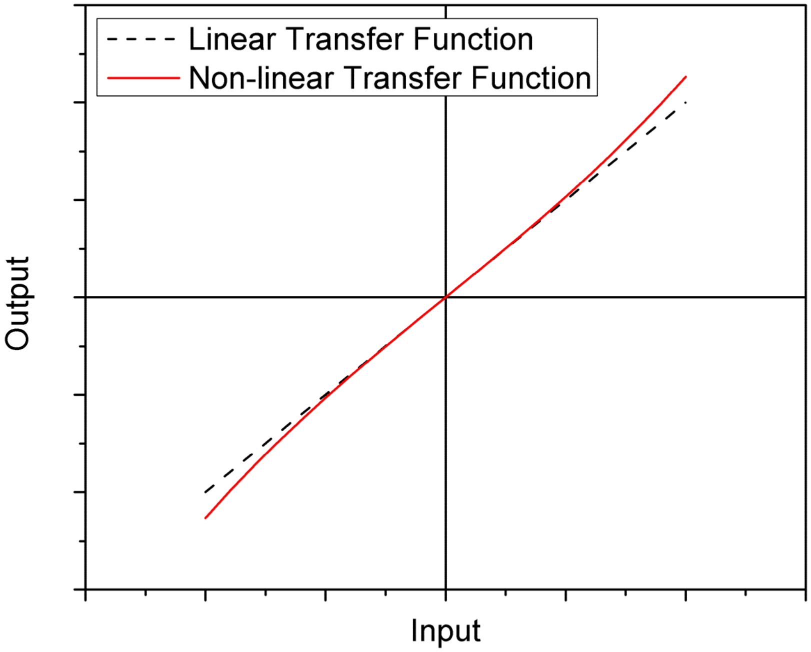

Figure 4.2: Sketch of a linear (black dashed line) and non-linear (red solid line) transfer function. In general, a non-linearity in a transfer function is any deviation from a straight line.

4.2 *Wheatstone Bridge*

Common-mode cancellation refers to techniques by which joint frequency components of two different signals are attenuated. As such, certain frequency components of a given signal can be filtered out by comparing the signal to a reference signal containing the same frequencies.

The cancellation can be achieved using a Wheatstone bridge coupled to the differential input of the lock-in amplifier with a high common mode rejection ratio (CMRR) of 100 dB (Figure 4.3). If the heater is the only element in the bridge which generates a third harmonic voltage, then balancing the bridge will attenuate the fundamental signal to −100 dB (10 ppm) without affecting the 3ω frequency component. It can be shown that the third harmonic of the Wheatstone bridge output $(W_{3\omega})$ is related to the 3ω voltage $(V_{h,3\omega})$ as

$$W_{3\omega} = \frac{R_1}{R_{h,0} + R_1} V_{h,3\omega}, \tag{3.2}$$

where $R_{h,0}$ is the room temperature resistance of the specimen heater and R_1 is the value of the in-series resistor in Figure 4.3. Therefore, from (2.49), the in-phase 3ω Wheatstone bridge output can be related to the thermal excitation frequency as

$$W_{3\omega}(2\omega) = -\frac{V_{h,0}^3 \beta_h}{4\pi l_h k R_{h,0}} \left(\frac{R_1}{R_{h,0} + R_1} \right) \left(\ln(2\omega) + \ln\left(b_h^2/\alpha\right) - 2\xi + i\,\pi/2 \right). \tag{3.3}$$

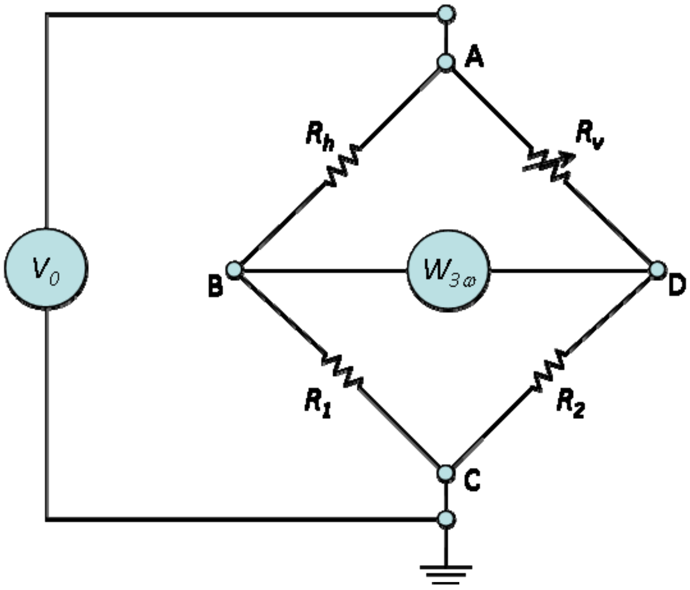

Figure 4.3: Schematic diagram of the Wheatstone bridge common-mode cancellation method. R_h is the heater, R_v is the variable resistor, V_0 is the fundamental signal from the function generator and $W_{3\omega}$ is the differential output voltage sent to the lock-in amplifier.

In order to satisfy the assumption of zero stray 3ω voltage, the resistors in the bridge are selected to have a TCR of less than 1% (−40 dB) of that of the heater. In addition, with the Wheatstone bridge one is able to control the amount of current passing in each arm of the bridge. By selecting the resistance of R_1 to be 100 times smaller than R_2, it is possible to direct 99% of the current through specimen arm of the bridge—points ADC in Figure 4.3—thus generating a relatively large 3ω voltage signal across the heater, while further minimizing any spurious third harmonic generation in the variable resistor by −40 dB (since $V_{h,3\omega} \propto I_h^2$). As such, the error in the third harmonic signal due to spurious signals produced by the elements of the bridge is on the order of −80 dB or 100 ppm.

4.3 *Lock-In Amplifier*

The 3ω voltage signal was measured using a lock-in amplifier (Stanford Research Systems SRS830), which is a device that can accurately measure the amplitude and phase of very small voltage or current signals. By using a technique called phase-sensitive detection, extremely narrow bandwidth filtering can be achieved, which enables very weak signals to be measured despite large amounts of noise. In our case, the "noise" is the fundamental signal itself, whose amplitude is roughly 3 orders of magnitude larger than the 3rd harmonic of the heater voltage.

4.3.1 Phase-Sensitive Detector

Phase-sensitive detectors (PSD) require a frequency reference to which it "locks-in" on, hence the name: lock-in amplifier. Due to the orthogonality of sinusoidal signals, the average product of two signal components is zero unless their frequencies are the same. Thus, by multiplying a noisy signal by a reference signal at a given frequency, one obtains a signal that is proportional to the noisy signal at that frequency. Using product-to-sum trigonometric identities, the product can be rewritten as a DC signal and an AC signal at twice the reference frequency. Given

$$\begin{aligned} V_{signal} &= \sum_n V_{n\omega} \sin(\omega_n t) \\ V_{ref} &= V_{ref} \sin(\omega_{ref} t) \end{aligned} \tag{3.4}$$

then

$$\begin{aligned} V_{DSP1} &= V_{ref} \times V_{signal} \\ &= V_{ref} \sin(\omega_{ref} t + \phi_{ref}) \sum_n V_{n\omega} \sin(\omega_n t + \phi_n) \\ &= \frac{1}{2} \sum_n \begin{Bmatrix} V_{n\omega} V_{ref} \cos((\omega_{ref} - \omega_n)t + \phi_{ref} - \phi_n) + \\ V_{n\omega} V_{ref} \cos((\omega_{ref} + \omega_n)t + \phi_{ref} + \phi_n) \end{Bmatrix} \end{aligned} \tag{3.5}$$

If the DSP output is passed through a low-pass filter, the AC signals are removed. Given an arbitrarily low cut-off frequency, the only signal that will pass unattenuated will be the difference term of the signal component with the same frequency as the reference frequency—i.e., $V_{n\omega} V_{ref} \cos((\omega_{ref} - \omega_n)t + \phi_{ref} - \phi_n)$ for $\omega_{ref} = \omega_n$. The AC signal is then removed using a low-pass filter and the reference voltage is divided out. As a result, the output of the DSP is a DC signal proportional to the magnitude of the noisy signal at the reference frequency given by

$$V_{DSP1} = V_{n\omega}\cos\left(\phi_n - \phi_{ref}\right). \tag{3.6}$$

However, the output of a single phase-sensitive detector will measure the in-phase component of the signal with the reference. In order to determine the magnitude of the signal, a second DSP is used with a reference signal phase angle of 90° from the first, yielding the out-of-phase component. Combining the two, the magnitude and phase angle can be obtained

$$\begin{gathered}
V_{DSP2} = V_{n\omega}\cos\left[\phi_n - \left(\phi_{ref} + \pi/2\right)\right] = V_{n\omega}\sin\left(\phi_n - \phi_{ref}\right) \\
R = \sqrt{V_{DSP1}^2 + V_{DSP2}^2} \\
\left(\phi_n - \phi_{ref}\right) = \tan^{-1}\left(\frac{V_{DSP2}}{V_{DSP1}}\right)
\end{gathered} \tag{3.7}$$

where

$$\begin{gathered}
V_{DSP1} \equiv V_X \\
V_{DSP2} \equiv V_Y
\end{gathered}$$

4.3.2 Low-Pass Filter

As mentioned above, a low-pass filter is used to eliminate the AC components from the lock-in amplifier output. Ideally, a low-pass filter would behave like a downward step function, completely attenuating the AC signals while passing the DC signal untouched; unfortunately this is not physically achievable. There are two parameters which dictate the performance of low-pass filters: roll-off rate (ROR) and cut-off frequency $\left(f_c\right)$ (Figure 4.4).

Roll-off rate represents the rate at which the power of the filtered signal decays above the cut-off frequency. High roll-off rates are needed especially at low excitation frequencies, as the AC signals become difficult to discriminate from the DC signal. The filter in the lock-in amplifier has a programmable roll-off rate of −20, −40, −60 or −80 dB/decade (One decade represents a tenfold increase in the frequency). The different roll-off rates are achieved by cascading (placing in series) up to four stages of filtering. For all the data collected in this work, the maximum roll-off rate of −80 dB/decade was used, representing an attenuation of ~16 times at $2f_c$.

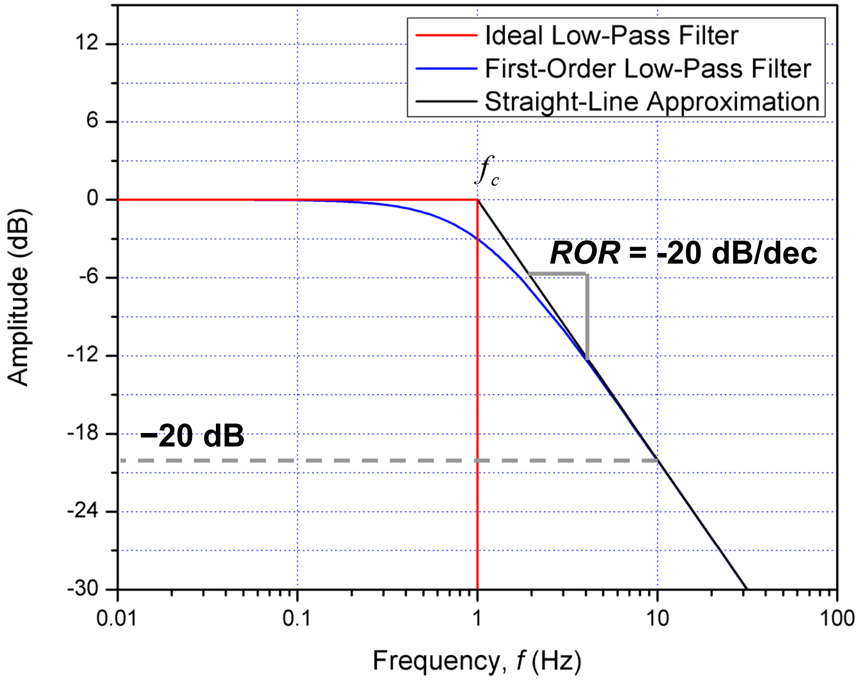

Figure 4.4: Bode plot of a low-pass filter (blue line), its straight line approximation (black line) and an ideal low-pass filter with an infinite roll-off rate (red line). The cut-off frequency is defined as the point where the attenuation is −3 dB, i.e., 1Hz in this case. The roll-off rate (*ROR*) is −20dB/decade.

The other important filter parameter is the cut-off frequency (f_c) of the filter. The cut-off frequency is defined as the point where the signal has been attenuated by −3 dB (i.e., ~29% attenuation). Ideally, the lowest possible cut-off frequency is desired, to increase the attenuation of the 2ω signal; however, there is a trade-off between low cut-off frequency and the filter settling time. The low cut-off frequencies require a long time to reach steady-state (Figure 4.5), while a high f_c may not completely attenuate the AC signal lead to error in the measurement (Figure 4.6). The cut-off frequency is defined as

$$f_c = \frac{1}{2\pi\tau_F}, \tag{3.8}$$

where τ_F is the filter time constant.

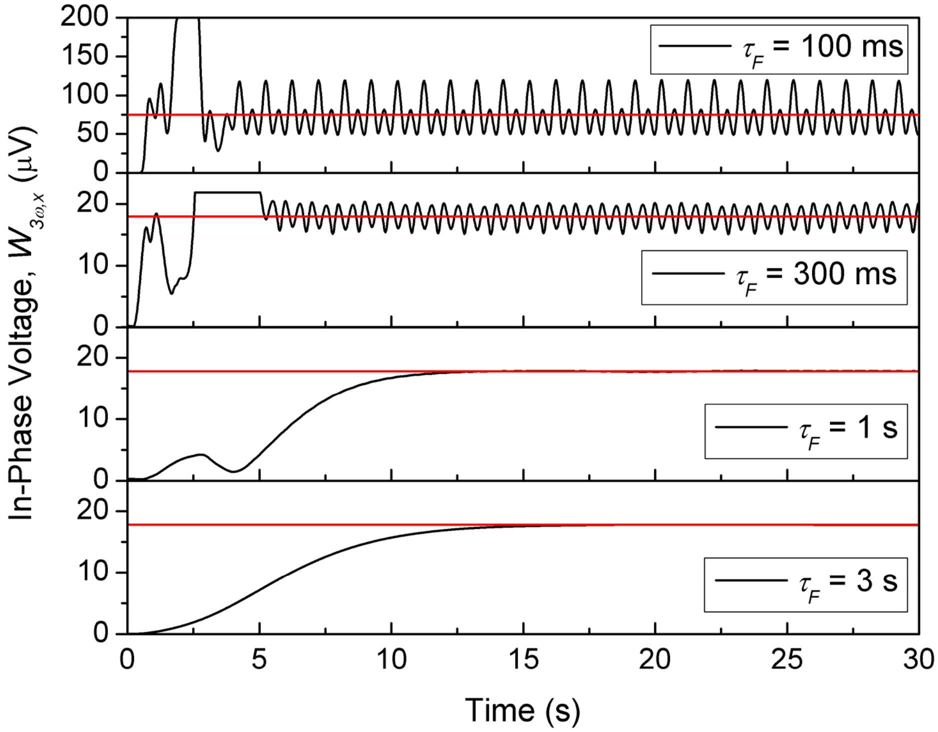

Figure 4.5: Time domain response of the in-phase lock-in amplifier output (black line) for different time constants. The red line represents the average stabilized voltage output. The excitation frequency is 1 Hz (2ω = 4π rad/s). As the time constant increases, the stabilization time and accuracy of the output increase.

The minimum time constant $\tau_{F,min}$ needed for a given attenuation (*x*, in dB) of the 2ω signal and a given roll-off rate (ROR), assuming straight-line approximation is

$$\tau_{F,min} = \frac{10^{x/ROR}}{2\omega} = \frac{10^{-x/80}}{2\omega}. \tag{3.9}$$

In order to maximize the accuracy of the output, a time constant of 10 seconds was chosen, such that the amplitude of the largest AC signal was less than the noise floor for the lowest signal frequency sampled (~1 rad/s). This represents a settling time of roughly 4 minutes. Given that the measurements were automated, these long testing times were not an issue. In addition, the long testing times do not seem to add any error due to drift. Experiments run over several days did not show any measurable change in the amplitude or phase angle of the 3ω voltage signal.

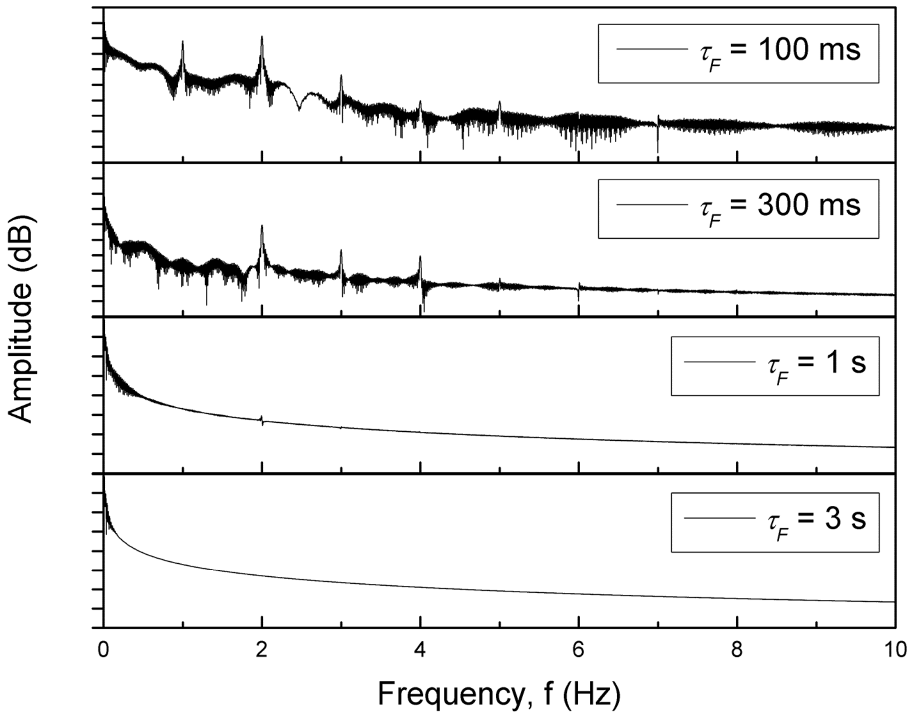

Figure 4.6: Frequency domain response of the lock-in amplifier output for different time constants. The excitation frequency is 1 Hz (2ω = 4π rad/s). As the time constant increases, the superfluous AC signal components are attenuated.

Even though the lock-in amplifier is designed to pick out small signals buried within large amounts of noise, the fundamental signal still required pre-attenuation prior to entering the lock-in amplifier. This is accomplished using the common-mode cancellation techniques presented above.

4.4 Experimental Procedure

In this section, we will describe the details of the experimental procedure used to conduct the 3ω measurements.

4.4.1 Specimen Mount

First, the specimen was placed on the mount base and silver paint was applied to the ends of the pogo pins. The pogo pins were carefully aligned above the heater contact pads. The Delrin® cross-beam was lowered until roughly 1 mm of spring travel remained—such that the spring was nearly fully compressed. The silver paint was left to dry in air for a period of no less than 30 minutes to ensure good electrical contact between the specimen heater and the pogo pins. The mount was then placed inside the vacuum chamber (Laco Technologies VHE Series), which was evacuated by a rotary vane vacuum pump (Adixen Pascal 2005 SD).

4.4.2 Wheatstone Bridge Balance

Next, an AC signal with a frequency of 1 kHz and the appropriate voltage amplitude was turned on and the Wheatstone bridge was balanced by adjusting the resistance of the variable resistor such that the differential ω Wheatstone bridge voltage was zero. This high balancing frequency was chosen so that the response time of the lock-in amplifier was kept short (i.e., short time constant) while maintaining an accurate reading. Due to the small DC temperature change, the Wheatstone bridge tends to drift out of balance. It was found that the drift in the differential Wheatstone bridge voltage fell to a negligible level after approximately 6 hours—such that the 3ω voltage is stable.

4.4.3 3ω Measurement

After the specimen reached thermal equilibrium and the Wheatstone bridge was balanced, the lock-in amplifier reference frequency was switched to monitor the 3rd harmonic. The function generator then iterated through a series of pre-programmed frequencies as the lock-in amplifier records the in-phase $(W_{3\omega,x})$ and out-of-phase $(W_{3\omega,y})$ voltages as well as the voltage magnitude $(|W_{3\omega}|)$ and phase lag (ϕ).

4.4.4 TCR Measurement

The TCR measurement was accomplished following the 3ω measurement. First, the specimen was removed from the mount to have freer access to the heater. A piece of adhesive tape was placed overtop the heater without covering the contact pads. Then, a type K thermocouple (National Instruments 9211) positioned above the heater and secured in place with more adhesive. The specimen was then re-mounted as above. Once the silver paint was dry, the mount was placed on a hot plate. The resistance of the heater was recorded using a digital multimeter (Agilent 34410A). Measurements were recorded when both the temperature and resistance measurements appeared stable for at least 5 minutes. This took on average 30 minutes for a 2 K temperature increase.

4.5 Conclusions

In the next chapter, we will conduct 3ω measurements on a well characterised reference specimen to validate the theoretical approach developed in Chapter 2. Statistical error analysis will also be performed to explore the accuracy, precision and repeatability of the 3ω apparatus.

Chapter 5: Validation of the 3ω Apparatus

In order to validate the mathematical model developed in Chapter 2, and the instrumented apparatus described in Chapter 3, a specimen with a well-known, low value of thermal conductivity was investigated. The material chosen was a monolithic fused quartz specimen measuring 1 mm in thickness.

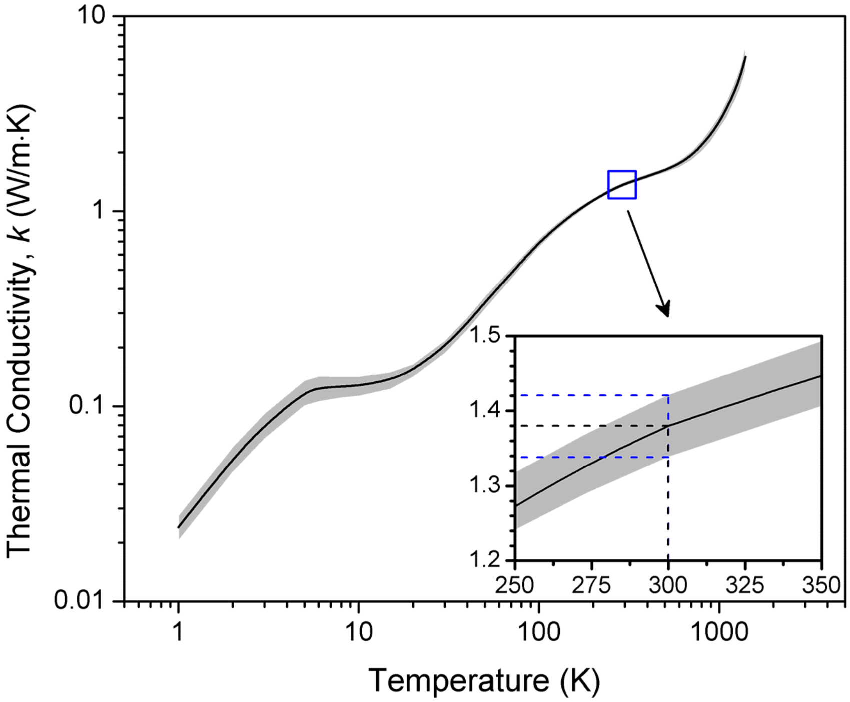

Figure 5.1: Thermal conductivity as a function of temperature for fused quartz from (Touloukian 1973). The uncertainty in the curve is indicated by the greyed region. Inset is a magnification of the temperatures in the neighbourhood of 300 K.

Fused quartz is commonly used to validate thermal conductivity measurement apparatus (Abdulagatov et al. 2000). It is an extremely pure amorphous polymorph of silicon dioxide (commercially available at >99.997% purity) with a well characterized thermal conductivity of 1.38±0.04 W/m·K at 300K (Touloukian 1973) (Figure 5.1). Due to the small amount of well defined trace impurities and well documented thermal properties, fused quartz makes for an excellent reference specimen to validate the accuracy of the experimental setup.

5.1 Linear Regression Analysis

Assuming that the approximate solution developed in Chapter 2 is correct, we hypothesise that the in-phase component of the Wheatstone bridge output $\left(W_{3\omega,x}\right)$ is proportional to the logarithm of the thermal excitation frequency (2ω) over a restricted frequency domain—the linear regime. This relationship is given by the real part of (3.3)

$$W_{3\omega,x}(2\omega) = -\frac{V_{h,0}^3 \beta_h}{4\pi l_h k R_{h,0}} \left(\frac{R_1}{R_{h,0} + R_1} \right) \left(\ln(2\omega) + \ln\left(b_h^2/\alpha\right) - 2\xi \right), \tag{5.1}$$

which is of the form

$$y = A + Bx, \tag{5.2}$$

where

$$\begin{aligned} x &= \ln(2\omega) \\ y &= W_{3\omega,x} \\ A &= B\left(\ln\left(b_h^2/\alpha\right) - 2\xi\right) \\ B &= -\frac{V_{h,0}^3 \beta_h}{4\pi l_h k R_{h,0}} \left(\frac{R_1}{R_{h,0} + R_1} \right) \end{aligned} \tag{5.3}$$

In Chapter 2, the linear regime boundaries were given as functions of the thermal penetration $\left(t_s/5 > \lambda > 5b_h\right)$. However, the thermal diffusivity of the specimen is unknown in general; therefore the thermal penetration depth

$\left(\lambda = \sqrt{\alpha/2\omega}\right)$ cannot be determined. As such, we require an alternative approach for estimating the boundaries of the linear regime. In this work, the boundaries of the linear regime were approximated—by inspection—as the *constant region of the out-of-phase Wheatstone bridge data* (Figure 5.2).

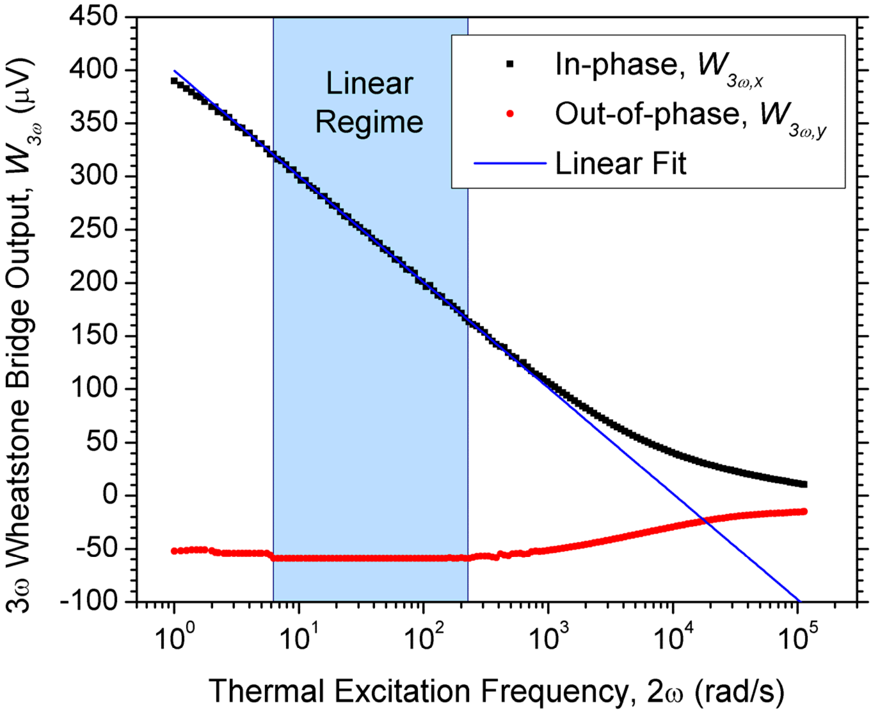

Figure 5.2: 3ω Wheatstone bridge outputs vs. thermal excitation frequency for fused quartz (specimen #5, $p_{rms} \approx 0.75$ W/m, $b_h = 20$ um). The linear regime (light blue shaded region) is determined from the range of constant out-of-phase outputs (red circles). The linear fit (blue line) is made from the in-phase data (black squares) within this linear regime.

Given the paired, sampled data (x_i, y_i), we use the *method of least squares* to obtain estimates $(\hat{A}, \hat{B})$ on the unknown coefficients A and B. These estimates are then used to determine the thermal conductivity (k) and thermal diffusivity (α) of the specimen using (5.3). The best fit will be one that minimizes the variance of the error (σ_ε) between the fit $\left(\hat{y}_i = \hat{A} + \hat{B}x_i\right)$ and the sampled data (y_i)—thus the name least squares. From (Miller and Miller 1999), the coefficients are given by

$$\hat{B} = \frac{S_{xy}}{S_{xx}} = \frac{\sum_{i=1}^{N}(x_i - \bar{x})(y_i - \bar{y})}{\sum_{i=1}^{N}(x_i - \bar{x})^2} \tag{5.4}$$

$$\hat{A} = \bar{y} - \hat{B} \cdot \bar{x}\,, \tag{5.5}$$

where N is the total number of sampled data points in the regression. The mean values are defined as

$$\bar{x} = \frac{1}{N}\sum_{i=1}^{N} x_i\,, \tag{5.6}$$

$$\bar{y} = \frac{1}{N}\sum_{i=1}^{N} y_i\,. \tag{5.7}$$

The uncertainty in the coefficients is given by their sample standard deviation—which measures the average root mean square discrepancy between the data and the mean:

$$s_A = s_\varepsilon \sqrt{\frac{\frac{1}{N}\sum_{i=1}^{N} x_i^2}{S_{xx}}} = s_\varepsilon \sqrt{\frac{\frac{1}{N}\sum_{i=1}^{N} x_i^2}{\sum_{i=1}^{N}(x_i - \bar{x})^2}}\,, \tag{5.8}$$

$$s_B = \frac{s_\varepsilon}{\sqrt{S_{xx}}} = \frac{s_\varepsilon}{\sqrt{\sum_{i=1}^{N}(x_i - \bar{x})^2}}\,, \tag{5.9}$$

where (s_ε) is the error sample standard deviation:

$$s_\varepsilon = \sqrt{\frac{\sum_{i=1}^{N}\left[y_i - \left(\hat{A} + \hat{B}x_i\right)\right]^2}{(N-2)}}\,. \tag{5.10}$$

A closer look at (5.8) and (5.9) reveals their meaning. Equation (5.9) states the uncertainty in the slope is proportional to the scatter in the data about the regression line, divided by the square root of the variance in *x*. As such, the estimate of slope will improve if the scatter in the data decreases or if we sample the data points farther apart. In addition, the estimate of the y-intercept will also improve if the data points are taken closer to the origin.

Lastly, the "goodness" of the fit is evaluated with the coefficient of determination $\left(\rho_{xy}^2\right)$, which is given by the ratio of the sample variance over the fit variance:

$$\rho_{xy}^2 = \frac{S_{yy}}{S_{\hat{y}\hat{y}}} = \frac{\sum_{i=1}^{N}\left(y_i - \bar{y}\right)^2}{\sum_{i=1}^{N}\left(\hat{y}_i - \bar{\hat{y}}\right)^2}, \tag{5.11}$$

where the best fit mean $\left(\bar{\hat{y}}\right)$ is given by

$$\bar{\hat{y}} = \frac{1}{N}\sum_{i=1}^{N} \hat{A} + \hat{B}x_i = \hat{A} + \hat{B} \cdot \bar{x} = \bar{y}. \tag{5.12}$$

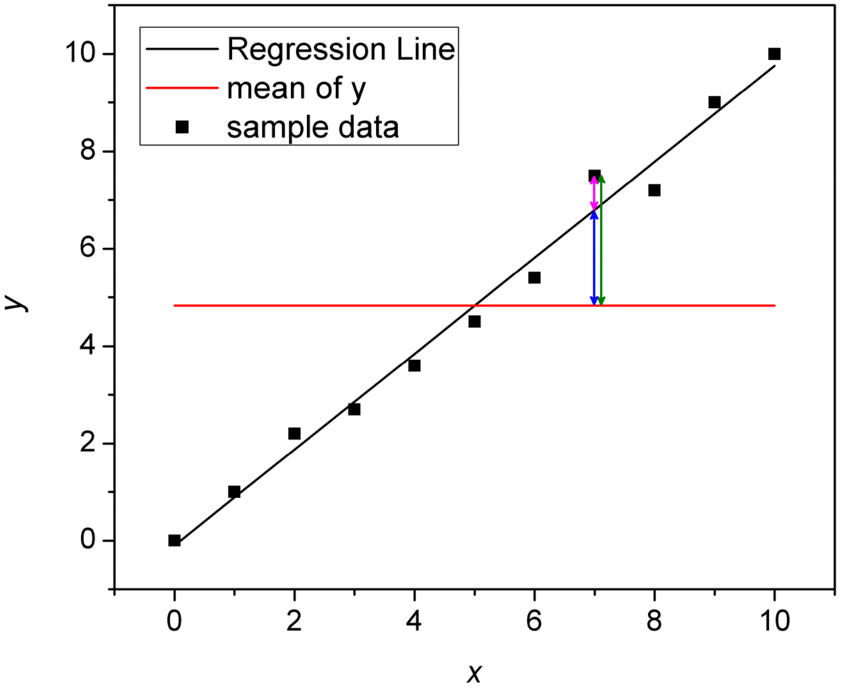

Figure 5.3: Sketch of linearly correlated paired data (black squares) along with the least squares best fit and mean value. The coefficient of determination indicates how much of the variation in *y* (represented by the green arrow) is accounted for by the regression line (blue arrow). The magenta arrow represents the unaccounted for variation.

Thus, the coefficient of determination measures how much of the total variation in y (green arrow) is accounted for by the fit (blue arrow) (Figure 5.3). A ρ_{xy}^2 value of 100% means there is no unaccounted for error—the length of the magenta arrow reduces to zero for all data points—and we are able to exactly predict the value of y for any unknown x within the interval $[x_1, x_N]$. The coefficient of determination for the linear fit in Figure 5.2 is 99.91%, indicating a very good fit to a straight line within the frequency range of constant out-of-phase outputs. Similar results were obtained for all of the fused quartz specimens (Table 5.1). Therefore, we assert that *the frequency range of constant out-of-phase 3ω Wheatstone bridge output is a good indicator of the linear regime*.

Table 5.1: Summary of the linear least squares curve fitting results for fused quartz for $p_{rms} \approx 0.75$ W/m. *N* is the number of data points used to fit the regression line.

Specimen #	N	ρ_{xy}^2	$\hat{A}$ (μV)	s_A (μV)	$\hat{B}$ $(\mu\text{V}/\ln(\text{rad/s}))$	s_B $(\mu\text{V}/\ln(\text{rad/s}))$
1	72	99.93	408.6	0.5	-43.0	0.1
2	35	99.91	404.9	0.9	-42.7	0.2
3	51	99.93	372.0	1.1	-40.0	0.4
4	60	99.94	378.2	0.5	-40.7	0.1
5	51	99.94	399.7	0.6	-43.2	0.2
6	55	99.94	362.5	0.5	-39.8	0.1

5.2 Additional Measurements

In order to deduce the thermal conductivity and thermal diffusivity from the estimates for slope and y-intercept in the linear regime, we must measure other physical parameters as indicated in equation (5.3). Unfortunately, not all of these parameters could be measured directly, such as the fundamental heater voltage, the heater resistance and TCR. In this section, we will describe the procedures used for these non-trivial property measurements.

5.2.1 Fundamental Voltage

In determining the thermal conductivity of the specimen, we require the peak amplitude of the nominal heater voltage $(V_{h,0})$. This quantity can be measured using either a voltmeter or the lock-in amplifier. The advantage of the lock-in amplifier is that it is able to discriminate between different harmonics, thus eliminating the contributions at higher harmonics due to heating and noise. Unfortunately, its maximum range is limited to 1 V_{rms}. A simpler approach would be to use a voltmeter (Agilent 34410A multimeter) to measure the total rms heater voltage $(V_{h,rms})$, which is given by

$$V_{h,rms} = \sqrt{\frac{1}{\tau}\int_0^{\tau} V_h^2(t)dt} \ ,$$

where

$$V_h(t) = V_{h,0}\begin{bmatrix} (1+\beta_h|\varDelta T_{DC}|)\cos(\omega t) + \tfrac{1}{2}\beta_h|\varDelta T_{AC}|\cos(\omega t+\phi) \\ +\tfrac{1}{2}\beta_h|\varDelta T_{AC}|\cos(3\omega t+\phi) \end{bmatrix} + \sum_{n=1}^{\infty} V_{n\omega}\, cos(n\omega t) \qquad (2.9)$$

and $V_{n\omega}$ is the voltage amplitude of the nth harmonic generated by the function generator.

5.2.1.a Total Heater Voltage Error Estimation

In order to simplify the measurement process, the fundamental voltage across the heater is estimated using the rms heater voltage measured by a digital multimeter. Discrepancies between the rms voltage and the fundamental voltage arise due to higher harmonic voltage contributions from the Joule heating in the heater and the harmonic noise produced by the function generator.

In order to mitigate the effects of the Joule heating, the rms voltage was measured at an excitation frequency of 1 kHz (~10^4 rad/s)—where the magnitude of the 3ω Wheatstone bridge output is small (Figure 5.2). Integrating, one obtains

$$V_{h,rms}=\sqrt{\frac{1}{2}\left(V_{h,0}^2\left(1+\beta_h^2\left(\left|\Delta T_{DC}\right|^2+\left|\Delta T_{AC}\right|^2\right)\right)+\sum_{n=1}^{\infty}V_{n\omega}^2\right)}. \tag{5.13}$$

Since the TCR of Gold is $\sim O\left(10^{-3}\right)$ and the temperature change was always less than 1K, the rms voltage due to the heating effects is negligible:

$$V_{h,rms}\approx\sqrt{\frac{1}{2}\left(V_{h,0}^2+\sum_{n=1}^{\infty}V_{n\omega}^2\right)}=\left(\frac{V_{h,0}}{\sqrt{2}}\right)\sqrt{1+\sum_{n=1}^{\infty}V_{n\omega}^2\Big/V_{h,0}^2}\;. \tag{5.14}$$

Given that the nominal heater voltage is a sinusoidal waveform, it is possible to define an rms nominal heater voltage as

$$V_{h,0,rms}=\sqrt{\frac{1}{\tau}\int_0^{\tau}V_{h,0}^2(t)dt}=\sqrt{\frac{\omega}{2\pi}\int_0^{2\pi/\omega}V_{h,0}^2\cos^2(\omega t)dt}=\frac{V_{h,0}}{\sqrt{2}}. \tag{5.15}$$

From (3.1), we recognise the second term under the square root in (5.11) as simply the total harmonic distortion (THD) of the function generator—given as 0.04% in the product data sheet—such that (5.15) can be expressed as

$$\frac{V_{h,rms}}{V_{h,0,rms}}=\sqrt{1+\mathrm{THD}}\,. \tag{5.15}$$

Therefore, the overestimation error introduced by using the total voltage rather than the nominal voltage is

$$(\%\mathrm{error})=\frac{\left|V_{h,rms}-V_{h,0,rms}\right|}{V_{h,0,rms}}\times 100\%=\left(\sqrt{(1+\mathrm{THD})}-1\right)\times 100\%=0.02\%. \tag{5.16}$$

As such, the error is negligible and we can consider the total heater voltage to be a perfect sinusoidal wave with a peak voltage given by

$$V_{h,0}\approx V_{h,rms}\sqrt{2}\,. \tag{5.17}$$

Comparative measurements using both the digital multimeter and the lock-in amplifier have shown that the actual difference between the two measurements is approximately 0.1% at an excitation frequency of 1 kHz.

5.2.2 Specimen Heater Resistance

In Chapter 2, we approximated the oscillating component of the power dissipated by the specimen heater via Joule heating as

$$P_{AC}(t) = \tfrac{1}{2} I_{h,0}^2 R_{h,0} \cos(2\omega t) = \frac{V_{h,0}^2}{2R_{h,0}} \cos(2\omega t). \tag{5.18}$$

However, the room temperature resistance does not take into account the small shift in resistance due to the DC heating. A better estimate of the power dissipated by the heater can be obtained using the rms resistance of the heater when the current is on (R_h). Unfortunately, resistance cannot be measured when an external potential difference is applied to the resistor. When the function generator is shut off, the resistance decays as the heater cools, making an accurate measurement difficult. Instead, the resistance of the parallel variable resistor—whose TCR is negligible—is measured with the digital multimeter and the heater resistance is deduced from Kirchhoff's voltage law applied to the balanced Wheatstone bridge:

$$R_h = R_v \frac{R_1}{R_2}, \tag{5.19}$$

where R_1 and R_2 are the in-series resistors whose resistances were measured before hand.

5.2.3 Temperature Coefficient of Resistance

In order to deduce the thermal conductivity from the slope of the linear regression curve $(\hat{B})$, we require the temperature coefficient of resistance (TCR) of the heater (β_h). TCR is defined as the fractional rate of change in resistance of the heater as a function of temperature:

$$\beta_h = \frac{1}{R_{h,0}} \frac{\partial R_h}{\partial T}. \tag{5.20}$$

Figure 5.4 shows a representative output from a TCR measurement of a Gold/chrome heater on a fused quartz specimen. Typical TCR measurement uncertainties were found to be approximately 1-6%. However, it is the systematic errors that are more of a concern, since they are difficult to quantify. Recall that the TCR measurement was accomplished by heating the Gold/chrome heater from below using a hot plate, while the temperature was monitored using a thermocouple placed overtop the line using adhesive tape. There are a number of problems with this setup.

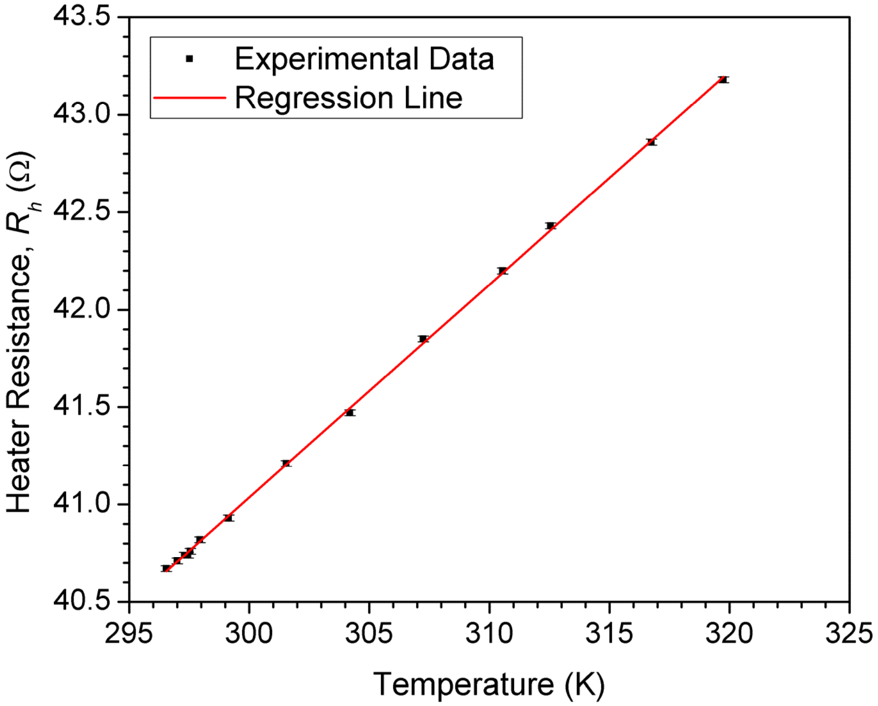

Figure 5.4: Resistance as a function of temperature of a Gold/chrome heater on a fused quartz specimen. The solid red line represents the linear regression curve using linear least squares.

First, it was found that the adhesive tape used to secure the thermocouple in place tended to lose tack at elevated temperatures, causing the thermocouple to lift off the surface. This would lead to downward drift in the temperature measurements and an overestimate of the TCR.

Second, for the heat to reach the metal line it must pass through the low thermal conductivity specimen. From the Wheatstone bridge balancing, it is known that it can take many hours for the specimen to reach thermal equilibrium, even for the small input power levels used for the 3ω measurements. Therefore it is possible that the heater is not in thermal equilibrium when the resistance measurements are recorded, leading to a systematic overestimation of the TCR.

Third, the specimen needed to be dismounted in order to fix the thermocouple on the heater. Therefore, the contact resistance between the pogo pins and the contact pads was different for the TCR measurements than for the 3ω measurements. Since the resistance was obtained via 2-wire resistance measurements, we were actually measuring the resistance of the heater and the leads, which include the lead wires, pogo pins, silver paint and contact pads. It is possible that the change in silver paint content had an effect on the recorded TCR.

Lastly, it is unknown whether the adhesive tape placed on the heater will affect future 3ω measurements with that specimen. Leaving the tape in place may affect the temperature field at the specimen surface while removing it may damage the heater. Therefore, the 3ω measurements were carried out first and the TCR experiments were treated as destructive tests—in that the specimens were no longer used afterwards.

5.2.3.a Alternative TCR Measurement Method

We have identified a number of issues related to the TCR measurement method which lead to an overestimate of the TCR and thus the thermal conductivity. In this section, we will describe an alternative method which would address these issues and decrease the systematic measurement errors.

All of these items were found to be related to the heating method—the hot plate. If instead, the metal heater is heated in a precise temperature-controlled oven—such that the heater is heated directly by the surrounding air, rather than through the specimen—then all of these problems can be minimized or avoided because the thermocouple no longer needs to be in direct contact with the heater. Therefore,

- The specimen heater will reach thermal equilibrium much quicker;
- No adhesive needs to be applied to the specimen heater, and;
- No drift in temperature due to movement of the thermocouple relative to the specimen heater.

5.3 Thermal Conductivity Results

Given the slope of the regression line and the other physical properties, we are now in a position to estimate the thermal conductivity of the fused quartz specimens. Figure 5.5 shows the best estimates of thermal conductivity for different quartz specimens (black squares) and their associated 95% confidence intervals (error bars). The black error bars represent the combined error from the 3ω and TCR measurements, while the blue error bars denote the 3ω measurement errors alone. The confidence interval represents the interval over which we are 95% certain that the thermal conductivity will lie (Miller and Miller 1999). The average measured value for the thermal conductivity of fused quartz using the 3ω apparatus was found to be 1.47±0.16 W/m·K—a 6% overestimation of the accepted value of 1.38 W/m·K. However, since each confidence interval for each measurement encompasses the accepted value, then the difference between each individual measurements and the benchmark is not *statistically significant* with 95% certainty.

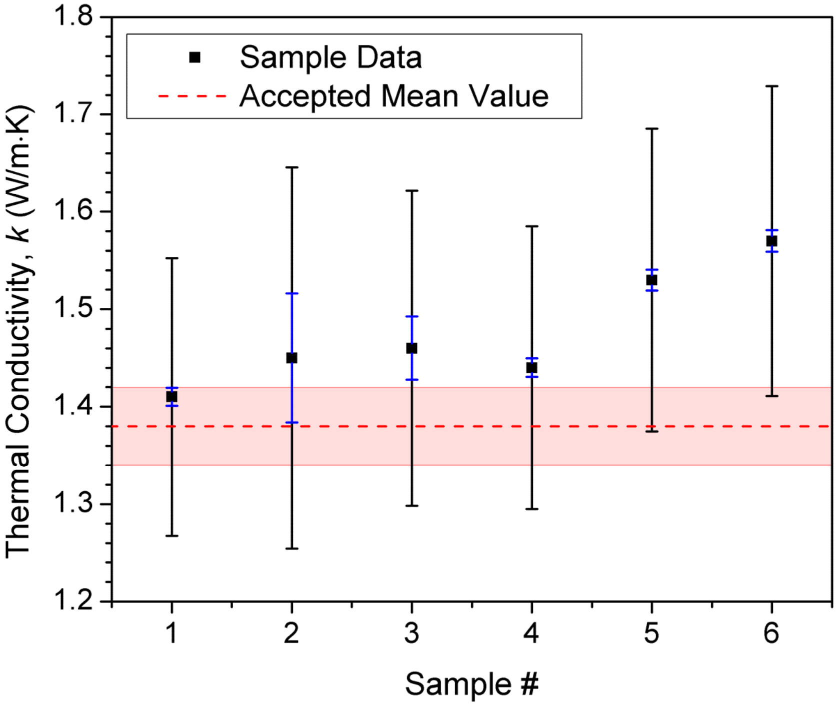

Figure 5.5: Measured thermal conductivity of fused quartz plates ($p_{rms} \approx 0.75$ W/m, $t_s = 1$ mm, $b_h = 20$ μm, $l_h = 8$ mm). The best estimates (black squares) are compared to the accepted value (red region) given in (Touloukian 1973). The black error bars represent the combined uncertainty (95% CI) from 3ω and TCR measurements, while the blue error bars denote the 3ω measurement errors alone.

However, a simple propagation of uncertainties analysis shows that roughly 97% of the error in thermal conductivity is due to uncertainty in the TCR of the Gold/chrome heater. If one disregards the TCR error, we find that the error in the slope of the regression line accounts for virtually 100% of the remaining total uncertainty in the thermal conductivity—i.e., the error from the other measurements is negligible. Since the 3ω measurements are independent of the TCR experiments, it is useful to perform a separate regression analysis without taking into account the TCR error (see section 5.4).

Given the estimates thermal conductivity and thermal diffusivity, the exact solution to the heat equation can be computed from (2.40)

$$\Delta T_h = \Delta T_{h,x} + i\Delta T_{h,y} = \frac{p_{rms}}{\pi k}\int_0^{\infty} \frac{\sin^2(\eta b_h)}{(\eta b_h)^2\sqrt{\eta^2 + q(\omega)^2}}\, d\eta\,, \tag{2.40}$$

where

$$p_{rms} = V_{h,0}^2 / 2 l_h R_{h,0}$$

$$q = \sqrt{2i\omega/\alpha}$$

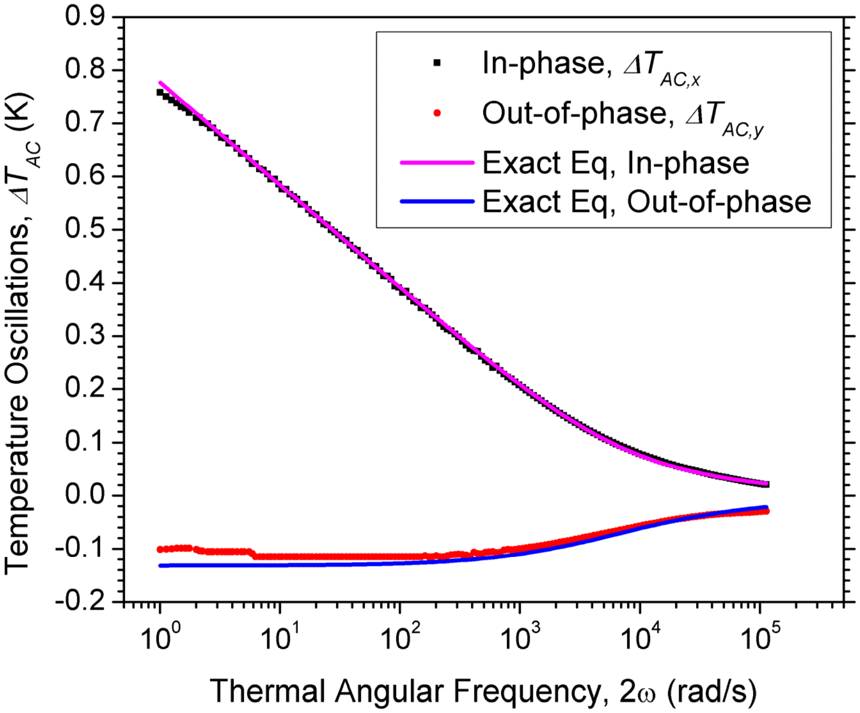

Figure 5.6: Amplitude of the temperature oscillations vs. thermal angular frequency. The discrete symbols represent the experimental data, while the lines are obtained from the exact analytical expression, i.e., equation (2.40).

The coefficients of determination for the in-phase and out-of-phase fits for specimen #5 are 99.97% and 76.38%, respectively (Figure 5.6). This close agreement validates the theoretical derivation outlined in Chapter 2. In addition, Figure 5.6 indicates that the magnitude of the out-of-phase response is not an accurate indicator of the specimen thermal conductivity compared to the slope of the in-phase response. This discrepancy seems to be systemic of the 3ω measurement technique (Cahill 1990).

5.4 Error Analysis

In this section we will attempt to identify and quantify the different sources of random and systematic error that affect the thermal property measurements using the 3ω apparatus.

5.4.1 Repeatability and Thermal Diffusivity Measurements

First, we would like to analyse the repeatability of the measurements for a given specimen at a fixed power level. Given that the amplitude of the temperature oscillations is a function of power level, we must rescale equation (2.47) as

$$\Delta\hat{T}_{AC,x}(2\omega) = \frac{\Delta T_{AC,x}(2\omega)}{p_{rms}} = -\frac{1}{2\pi k}\left(\ln(2\omega) + \ln\left(b_h^2/\alpha\right) - 2\xi\right). \tag{5.21}$$

Therefore, $\Delta\hat{T}_{AC,x}$ should be invariant for a given heater geometry. The most important contributing factor to the repeatability of the 3ω measurements is the value of the electrical interface resistance between the pogo pins and the contact pads. The electrical interface resistance is a function of the amount of silver paint applied to the pogo pins and the contact pressure applied by the mount—both of which are loosely controlled by visual inspection.

In order to determine if there is a statistically significant difference between the slope and y-intercept of the different regression lines, we perform an analysis of variance (Neter and Wasserman 1974). Basically, we compare the variance of the sum of the individual regression residuals to that of the pooled residuals: if the variances are similar—compared to an appropriate statistical distribution (i.e., *F*-distribution)—than the discrepancies in the regression lines are statistically insignificant. If the similarity hypothesis is false, then a *covariance* analysis (Neter and Wasserman 1974) is used to determine if the difference lies in the regression slopes or intercepts, or both. For both the variance and covariance analyses, we make the following reasonable assumption:

- Normality of error terms;
- Equality of error variances for measurements;
- Linearity of the regression.

The repeatability of the 3ω measurements was investigated by taking 3 separate measurements of specimen #2—completely dismounting each time—at an input power level of ~0.75 W/m (Figure 5.7).

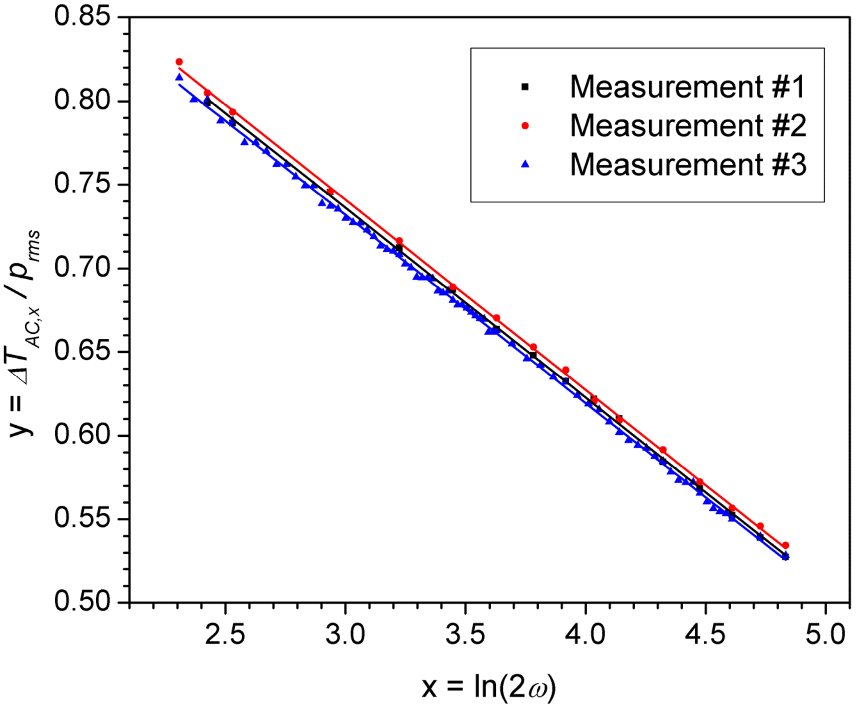

Figure 5.7: Rescaled in-phase temperature oscillations vs. the logarithm of the thermal excitation frequency. The different data sets denote separate measurements of the same specimen (specimen #2). The solid lines of the appropriate color represent the regression lines for the different measurements

Visual inspection of Figure 5.7 indicates that the y-intercept of the regression lines appear different. The covariance analyses confirmed that the differences in the y-intercepts were statistically significant $\left(F^* = 114 > 3.07 = F_{0.95,2,120}\right)$, while the slopes (i.e., thermal conductivities) were equivalent with a confidence of 95% $\left(F^* = 1.69 < 3.07 = F_{0.95,3,120}\right)$. This seems to indicate that the thermal conductivity measurements are immune to any repeatability issues with respect to the mounting of specimens for the 3ω apparatus. The same cannot be said for the thermal diffusivity (y-intercept). Therefore, *the 3ω apparatus is not appropriate for the measurement of the thermal diffusivity of the specimen*.

5.4.2 Specimen Variability

In section 5.3, we compared the measured thermal conductivities to a known benchmark, but we are also interested in determining the level of significance of the *variations between the specimens* themselves. Measuring the variability between specimens is done following the same procedure as in section 5.4.1 using the analysis of covariance. The measured data points (points) and their respective regression lines (solid lines) for the different fused quartz specimens are shown in Figure 5.8.

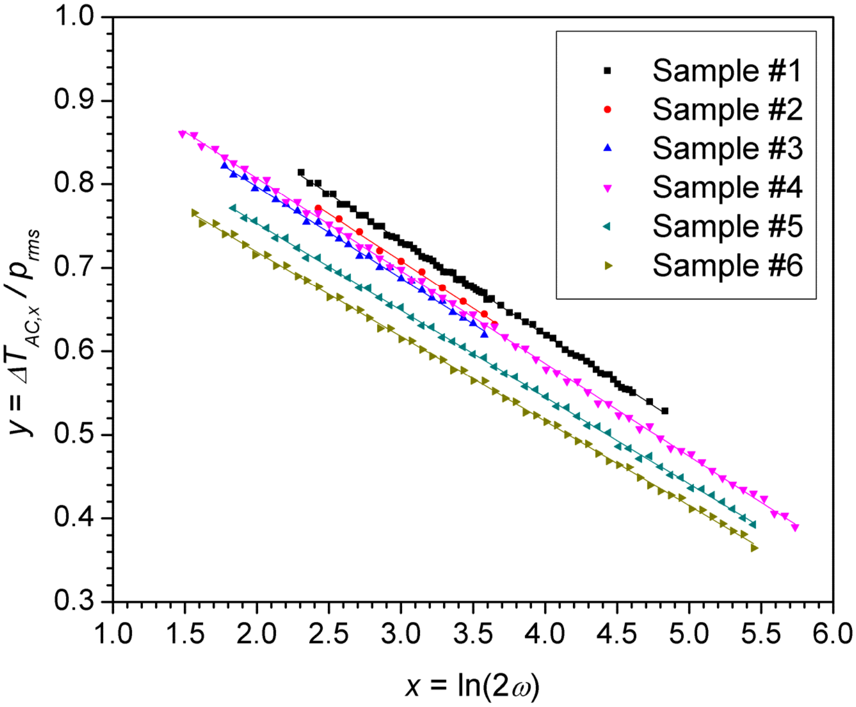

Figure 5.8: Linear regime data for the various fused quartz specimens along with their best fit regression lines ($p_{rms} \approx 0.75$ W/m).

The covariance analysis found that differences in the slope of the various measurements were statistically significant (Table 5.2). This can also be seen from the discrepancies in the confidence intervals (blue error bars) for the various thermal conductivity estimates in Figure 5.5. This may be due to variations in the individual heater TCRs or some other factor. Additional measurements confirmed that the gradual upward trend in measured thermal conductivity (Figure 5.5) is not due to drift with time.

Table 5.2: P-values for different fused quartz specimens

	F^*	$F_{0.95,5,\infty}$
Slope	155	2.21
Y-Intercept	3064	2.21

5.4.3 Low Frequency Divergence

The gradual divergence from the exact equation in both the in-phase and out-of-phase responses at low frequencies (Figure 5.6) is thought to be caused by the finite thickness of the specimen. Recall that the exact solution derived in Chapter 2 was for a semi-infinite solid and is valid only for thermal penetration depths much smaller than the thickness of the specimen. If we compute the thermal penetration depth (λ) for the different frequencies at an input power of ~0.75 W/m, we find that the lower bound for the linear regime is roughly 0.2 mm, or $1/5$ of the specimen thickness. Given that the heat decays exponentially through the specimen, one expects that the thermal wave will decay below 1% of its initial amplitude after 5 "length constants", i.e., 5 times the thermal penetration depth. This divergence from the exact equation is due to interference with reflected waves from the interface between the specimen and the mount.

5.4.4 Out-of-Phase Signal

Inspection of Figure 5.6—as well as the coefficient of determination—reveals that the fit of the exact equation to the out-of-phase temperature oscillations is not as good as for the in-phase response. One possible cause for this was the presence of stray reactance in the custom-built Wheatstone bridge circuit.

While balancing the Wheatstone bridge, a positive out-of-phase voltage signal was detected at the fundamental excitation frequency (ω). Given that a Wheatstone bridge contains only resistive elements, there should not be any out-of-phase fundamental voltage signal in the circuit at all. Therefore, any out-of-phase signal must be due to stray reactance, either capacitive or inductive. The positive stray reactance was found to increase linearly with frequency (Figure 5.9), indicating it was stray inductance.

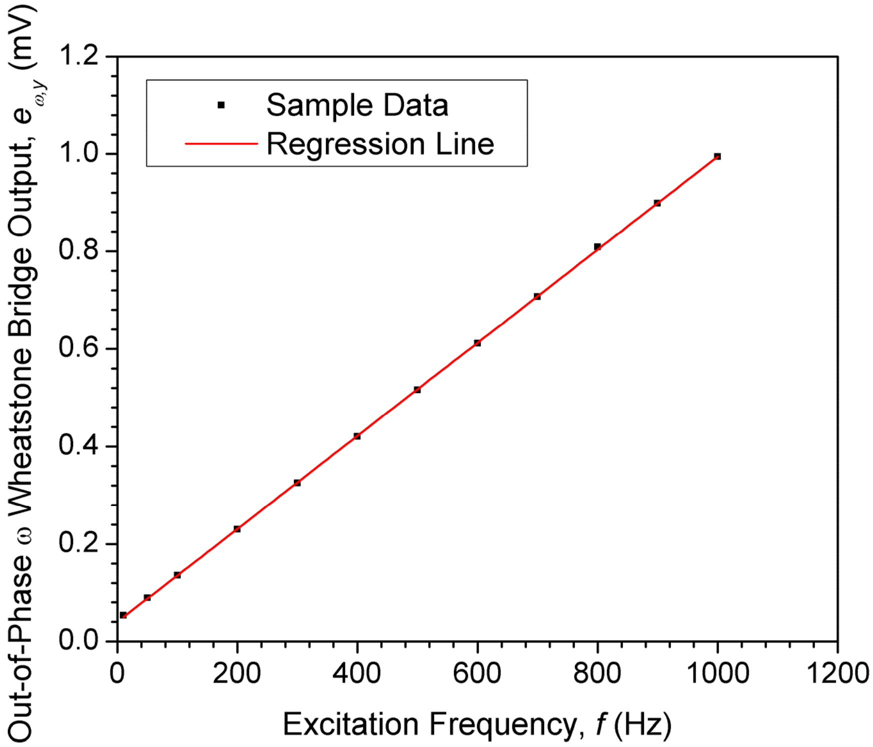

Figure 5.9: Amplitude of the out-of-phase fundamental voltage signal vs. excitation frequency due to stray inductance in the specimen arm of the Wheatstone bridge. Given the magnitude of the current in the specimen arm, the inductance was found to be 73.2±0.1 mH.

Since the differential output was wired such that the potentiometer arm voltage was subtracted from specimen arm voltage, we know that a net positive inductance was coming from the specimen arm of the bridge, since one cannot have negative inductance (just like one cannot have negative resistance). Given the current passing through the heater and the frequency response of the out-of-phase voltage at ω, it was possible to deduce the impedance of the specimen arm as 73.2±0.1 mH. The stray inductance was systemic and probably due to either the vacuum chamber lead wires or the unshielded pogo pins used to make the electrical connections to the specimen. We wished to estimate the contribution of the stray out-of-phase voltage signal at ω on the out-of-phase 3ω voltage. Combining (2.10) and (3.2)

$$W_{3\omega} = \tfrac{1}{2}\beta_h V_{h,0} \varDelta T_{AC}\left(\frac{R_1}{R_{h,0}+R_1}\right), \tag{5.22}$$

where

$$\begin{aligned}
V_{h,0} &= V_{h,0,x} + iV_{h,0,y} \approx \left(W_{\omega,x} + i0\right)\left(\frac{R_{h,0}+R_1}{R_1}\right) \\
W_{3\omega} &= W_{3\omega,x} + iW_{3\omega,y} \\
\varDelta T_{AC} &= \varDelta T_{AC,x} + i\varDelta T_{AC,y}
\end{aligned}$$

Now, we correct the fundamental voltage to take into account the stray out-of-phase voltage yielding

$$V'_{h,0} = V_{h,0,x} + iV_{h,0,y} \approx \left(W_{\omega,x} + iW_{\omega,y}\right)\left(\frac{R_{h,0}+R_1}{R_1}\right).$$

Therefore, (5.7) gives

$$W_{3\omega,x} = \tfrac{1}{2}\beta_h\left(\frac{R_1}{R_{h,0}+R_1}\right)\left(V_{\omega,x}\varDelta T_{AC,x} - V_{\omega,y}\varDelta T_{AC,y}\right), \tag{5.23}$$

$$W_{3\omega,y} = \tfrac{1}{2}\beta_h\left(\frac{R_1}{R_{h,0}+R_1}\right)\left(V_{\omega,x}\varDelta T_{AC,y} + V_{\omega,y}\varDelta T_{AC,x}\right), \tag{5.24}$$

resulting in a maximum error of 0.25 μV at a frequency of 9 kHz (or $2\omega \approx 10^5$ rad/s). Therefore, the contribution from the stray inductance on the amplitude of the out-of-phase 3ω voltage was negligible.

5.4.5 Effect of Input Power

In Chapter 2, we defined the linear regime as a range of frequencies for which the associated thermal penetration depth is less than $\frac{1}{5}$ the thickness of the specimen, but greater than 5 times the half-width of the heater $\left(t_s/5 > \lambda > 5b_h\right)$. The lower limit is rather straightforward: if the thermal wave exceeds the thickness of the specimen, than the resultant thermal properties will be a composite of the specimen and the mount. The upper limit is more arbitrary: when the thermal penetration depth decreases beyond a certain point (i.e., the frequency increases), the frequency response of the temperature oscillations (i.e., the Bessel function) deviates from linearity (Figure 5.2). This deviation is gradual, but a clear function of the heater half-width; as such we arbitrarily set an upper limit on the linear regime as 5*b*, resulting in a maximum error in the slope of the linear regime of less than 1%. It was found that the observed plateau in the out-of-phase 3ω voltage did not always coincide with these limits. For example, in Figure 5.2, the upper limit of the constant domain occurs at a thermal penetration depth of 56 μm, well beyond 5*b* (100 μm). The correspondence of the lower limit with $\frac{1}{5}$ of the specimen thickness was found to be pure chance. Rather, the extent of the constant plateau depends on the amount of power dissipated by the heater (P_0), such that the constant domain extends for lower power levels and disappeared completely at high power levels (i.e., $p_{rms} = 28\ \mathrm{W/m}$) (Figure 5.10).

For low input powers, the initial amplitude of the temperature wave is proportionally smaller, such that the effect of the reflected waves will only be felt by the heater if they are larger than the *resolution of the lock-in amplifier*. Therefore, at lower input powers, the finite thickness effects will only be recorded at larger thermal penetration depths—although the oscillations still decay at the same *rate*. Although there is a large amount of uncertainty in the data and the frequency step sizes are not uniform for all the data, Figure 5.10 seems to agree with this trend of shrinking linear regime with increasing power.

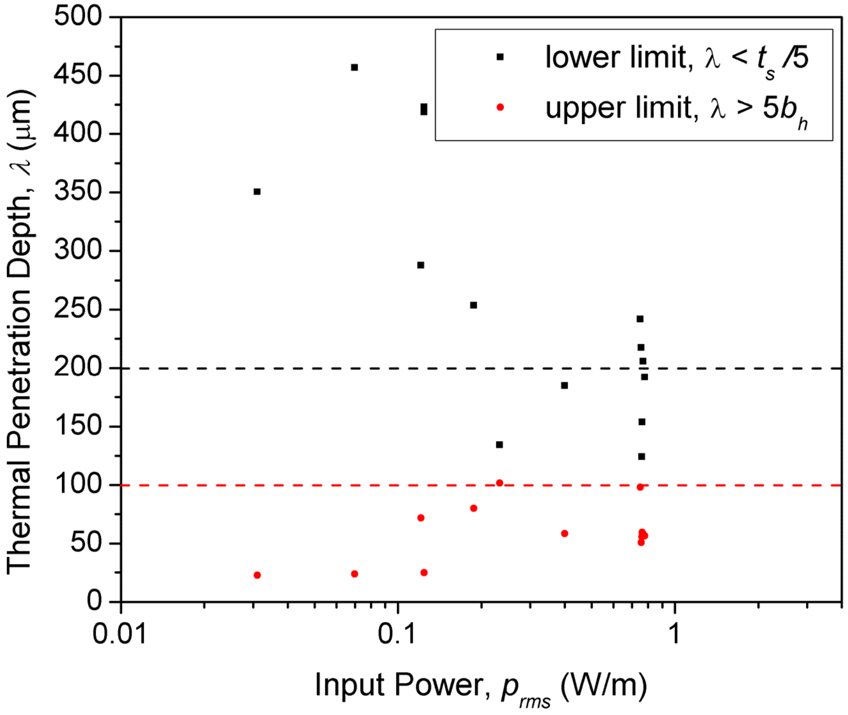

Figure 5.10: Linear regime boundaries as a function of input power level. The lower limit (with respect to thermal excitation frequency, 2ω) is shown in black squares and the upper limit is given red. The specimen thickness (t_s) is 1 mm and the heater half width (b_h) is 20 μm. The dotted lines indicate the boundaries based on the theory developed in Chapter 2 ($t_s/5>\lambda>b_h$).

For all measurements below 0.2 W/m, anomalous *staircase function behaviour* appeared in the linear regime of the in-phase 3ω voltage amplitude (Figure 5.11). Such behaviour has never been reported in the literature. In each measurement where the steps are visible, the vertical separation between the steps is constant within ~1%. Furthermore, when the voltage signals were converted into temperatures, the step heights appeared roughly in integer multiples of 5 mK, with the step size tending to increase with increasing power (Figure 5.12).

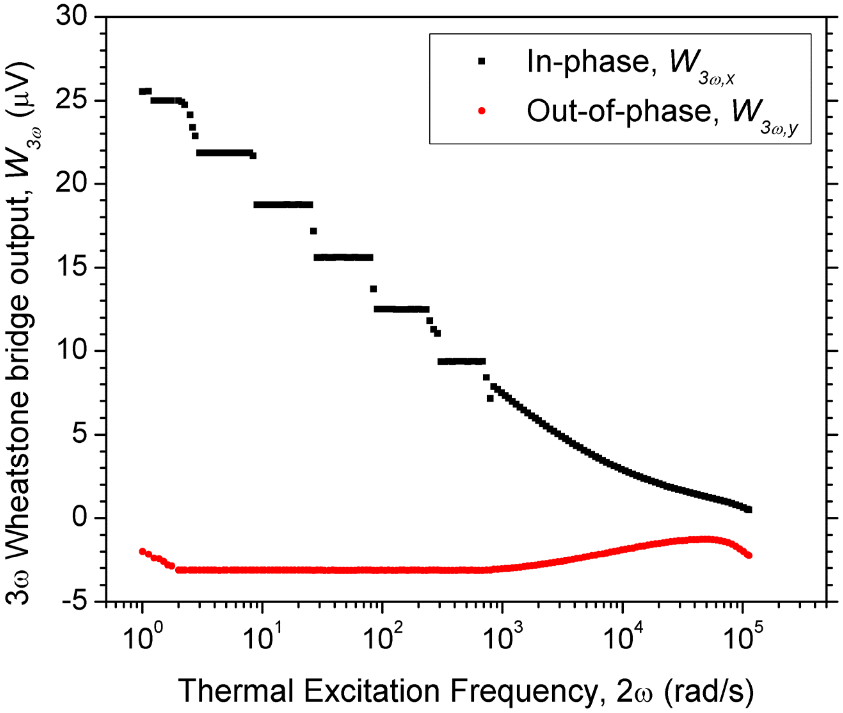

Figure 5.11: 3ω Wheatstone bridge outputs vs. thermal excitation frequency for fused quartz (p_{rms} = 0.12 W/m, b_h = 20 um). Staircase function behaviour was visible in the linear regime of the in-phase output for all input power levels below ~0.2 W/m.

Although not clearly visible in Figure 5.11 at low frequencies, the staircase regime was found to be bounded on both sides by smoothly decaying regions. The sudden transition from a staircase-like behaviour in the linear regime to a smooth decay in the transition regime clearly indicates that this behaviour is *not due to resolution limitations* in the apparatus, frequency-dependent or otherwise. In addition, the frequency range where the staircase effect was visible coincided almost exactly with the constant region in the out-of-phase output, raising doubts about the nature of the constant out-of-phase region.

One clue to the origin of the steps is the level of input power per unit heater length. The steps were visible in all measurements taken at power levels ranging from 30 to 800 mW/m. In contrast, most other groups reporting 3ω results used power levels roughly 3 orders of magnitude larger (30 to 800 W/m) (Kim et al. 1999; Alvarez-Quintana and Rodríguez-Viejo 2008). For the high power measurement taken at 28 W/m, no steps or linear regime were observed.

Nevertheless, the slope of the 3ω measurement regression lines showed no statistically significant difference with respect to the input power level—although this may simply be due to the larger error present at lower power levels (Figure 5.13).

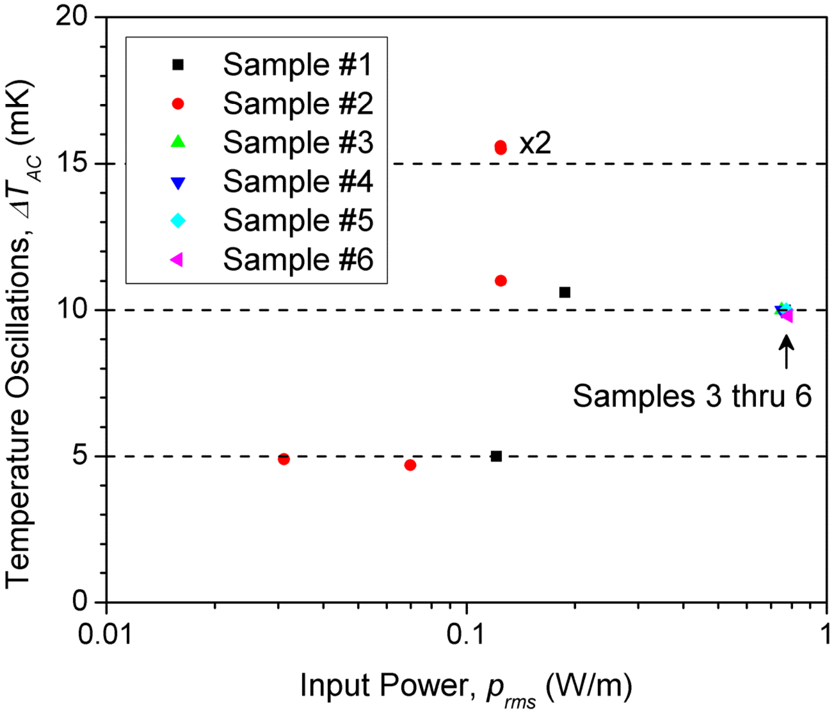

Figure 5.12: Vertical step height in the in-phase component of the temperature oscillations as a function of input power. All three observed step sizes were approximately integer multiples of 5 mK.

Indeed, the uncertainty in both the thermal conductivity and thermal diffusivity data was found to increase significantly with decreasing power. The correlation coefficients (ρ_{xy})—given by the square root of the coefficient of determination (ρ_{xy}^2)—were found to be −0.76 and −0.82 for the thermal conductivity and thermal diffusivity, respectively, for 18 fused quartz experiments conducted with different specimens and power levels. The probability that these correlations are incidental are less than 0.1% (Taylor 1997). However, one cannot increase the input power too high because the linear regime disappears completely at higher input power levels.

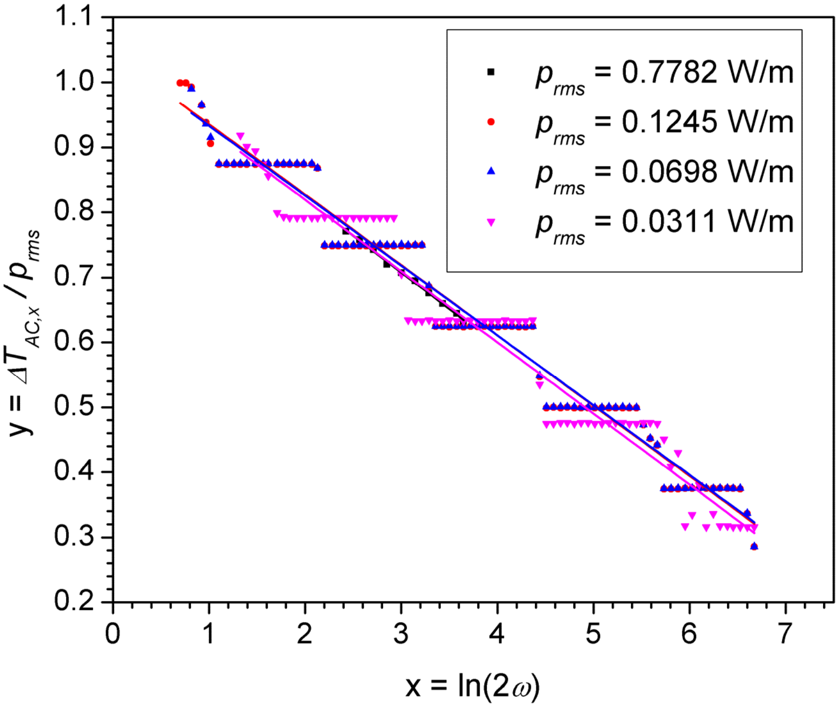

Figure 5.13: Linear regime data for fused quartz specimen #2 at different input power levels along with their best fit regression lines.

5.5 Conclusions

Using the 3ω technique, we have obtained an average thermal conductivity for fused quartz of 1.47±0.16 W/m·K, compared to the accepted value of 1.38±0.04 W/m·K. This represents a precision uncertainty of 10% and an average systematic overestimate error of 6%. Both of these errors have been shown to be associated to the TCR measurements. Therefore, in order to improve the accuracy and precision of the 3ω apparatus, a more reliable method of determining the heater TCR is required.

In addition, anomalous staircase behaviour in the linear regime of in-phase 3ω voltage response was observed. The size of the stairs was constant for a given measurement and was found to increase with decreasing input power. Furthermore, the step sizes were always found to be integer multiples of approximately 5 mK. Due to the large steps, the uncertainty in the slope of the linear regime—i.e., thermal conductivity—tended to increase with decreasing input power. This behaviour has never been reported before and casts doubts whether the 3ω measurements were conducted at too low input power. More measurements need to be taken at higher input power levels to confirm this.

On the other hand, the thermal diffusivity measurements from the y-intercept of the in-phase 3ω voltage response were found to be highly variable and unreliable. This was due to relatively large changes in the in-phase voltage response brought about by small changes in electrical interface resistance—due to changes in pogo pin clamping pressure and silver paint. Therefore, the thermal diffusivity measurements were not considered significant.

Given the positive results for fused quartz, other materials of interest for power harvesting microsystems were evaluated, namely Lead Zirconate Titanate (or PZT)—a material commonly used in vibration harvesters.

Chapter 6: Thermal Conductivity of PZT

In this section, we will present the initial thermal conductivity measurements for Lead Zirconate Titanate (PZT)—a piezoelectric ceramic material. Thermal conductivity data for PZT materials are of importance for the optimal design of microsystems for vibration energy harvesting. Specifically we investigated PZT-5A4E, a commercially available, polycrystalline sintered PZT. The only thermal conductivity information available from PZT material suppliers was a design value quoted as roughly 1.8 W/m·K—irrespective of composition. Only two studies on the thermal conductivity of PZT materials were found in the open literature (Yarlagadda et al. 1995; Kallaev et al. 2005).

Yarlagadda et al. investigated the thermal conductivity of two different *poled* PZT compositions (PZT-4S and -5H) from 15-300K using an absolute longitudinal plate method similar to the one outlined in Chapter 1. The thermal conductivity was measured in the poled direction. They found values of thermal conductivity of 0.14 and 0.18 W/m·K at 300K for PZT-5H and PZT-4S, respectively—more than one order of magnitude lower than the design value. However, they only measured one specimen of each material and no uncertainty estimates were reported.

Kallaev et al. studied the *unpoled* thermal conductivity of yet another type of PZT (PZT-19) over the temperature range 290-800K. The details of the measurement apparatus were not disclosed. A value of 2.0±4% W/m·K at 300K was interpolated from their experimental data.

Although the results reported by the above studies are not extensive, they seem to indicate a strong relationship between thermal conductivity and either PZT composition or poling. As a first step in investigating these possible relations, the thermal conductivity of *unpoled* PZT-5A4E was measured at room temperature using the 3ω apparatus.

6.1 Heater Fabrication

Due to its sintered nature, the PZT specimens had a non-negligible surface roughness, which could impact the continuity of the thin film heater and render thickness measurements difficult. Using the profilometer at the University of Sherbrooke microfabrication facility (Tencor Alphastep), the peak surface roughness was measured as 3.5 μm—an order of magnitude larger than the thickness of the heater.

The thickness of the metal films sputtered onto the PZT specimens was measured from a silicon witness specimen, patterned simultaneously with the PZT specimens. Optical microscopy indicated that the deposited heaters were continuous and electrical resistance measurements confirmed that no open circuits existed. However, the resistance of the heaters were almost three times higher than those deposited on the smooth fused quartz specimens. The increase in resistivity is believed to be due to increased electron boundary scattering from the rough surface (Namba 1970; Dubey et al. 1991).

6.2 Temperature Coefficient of Resistance

The change in resistivity of the Gold/chrome heaters motivated new measurements for the temperature coefficient of resistance (TCR) of the binary film on PZT (Warkusz 1987). The TCR of three randomly chosen PZT heaters were measured and found to be consistently smaller than on fused quartz by ~20% (Table 6.1). Assuming these three values are representative of the different specimens, an average TCR is computed and used to determine the thermal conductivity of the PZT specimens.

Table 6.1: Temperature coefficient of resistance (TCR) of three randomly chosen PZT specimen heaters.

Specimen #	TCR (K^{-1})	Uncertainty (95% CI)
1	0.00202	0.00004
6	0.00223	0.00016
8	0.00209	0.00006
Mean	*0.00211*	*0.00012*

6.3 Thermal Conductivity

Using the mean value of TCR from Table 6.1, the thermal conductivity of the different, *unpoled* PZT-5A4E specimens are given in Figure 6.1. The average thermal conductivity was found to be 1.38±0.10 W/m·K.

The analysis of variance determined that the thermal conductivity of the different specimens—assuming an average TCR—were significantly different with 95% confidence. The covariance analysis on the difference specimens showed that both the y-intercepts and slopes were significantly different (Table 6.2).

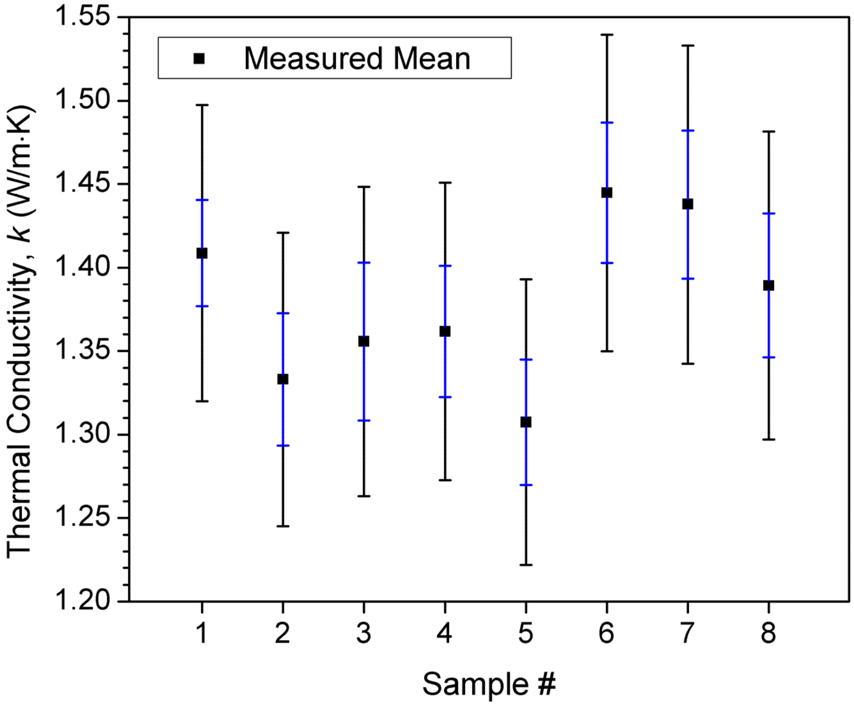

Figure 6.1: Measured thermal conductivity for PZT-5A4E. Total uncertainty (95% CI) is given by the black error bars, while the uncertainty without the TCR error is denoted by the blue error bars.

Table 6.2: Covariance analysis results for different PZT specimens

	F^*	$F_{0.95,7,120}$
Slope	8.73	2.39
Y-Intercept	139	2.39

6.4 Conclusion

Using the 3ω technique, the thermal conductivity of PZT-5A4E was found to be 1.38±0.10 W/m·K. Given that the value of thermal conductivity of fused quartz obtained from the combined 3ω and TCR measurements yielded a 6% overestimate on the accepted value found in the literature, it is possible that the thermal conductivity of PZT-5A4E lie closer to 1.30 W/m·K.

It seems to be a coincidence that the thermal conductivity of PZT-5A4E is very close to that of the quartz glass, rather than instrument error, where the device systematically yields the same result for all materials. The latter interpretation can be dismissed since the thermal conductivity measurement is obtained from two independent measurements: the slope of the voltage-frequency response (i.e., the 3ω measurement) and the TCR measurement. Given that the TCR of the PZT sample heaters was roughly 20% smaller than the quartz heaters, the 3ω measurements also differ by the same amount to yield similar thermal conductivities.

The thermal conductivity measurements of unpoled PZT-5A4E are on the same order of magnitude as the design value and that obtained by Kallaev et al. for *unpoled* PZT-19, but differ significantly from the values for poled PZT-4S and PZT-5H reported by Yarlagadda et al. This seems to indicate a particularly strong correlation between poling and thermal conductivity which warrants further investigation.

Chapter 7: Conclusion and Future Work

In this thesis, a thermal conductivity measurement apparatus was successfully designed, built and validated for measuring functional materials for use in power harvesting microsystems. The system makes use of the 3ω technique, which has been previously used to characterise a wide variety of materials. The apparatus was validated using a fused quartz, yielding a mean thermal conductivity of 1.47±0.16 W/m·K, in agreement with the accepted value of 1.38 W/m·K. The discrepancies in the mean values represent an overestimation error of 6%—which is a reasonable level of uncertainty for thermal conductivity measurements (Yang 2008).

Thermal conductivity is deduced by combining 3ω measurements with the temperature coefficient of resistance (TCR) measurements. It was found that a large majority of the uncertainty—97% for fused quartz—in the thermal conductivity results stem from the TCR measurements.

Next, the thermal conductivity of unpoled Lead Zirconate Titanate (PZT-5A4E) was investigated. It was found to have a thermal conductivity of 1.38±0.10 W/m·K. This value is 30% less than the value reported by Kallaev et al. for unpoled PZT-19 and an order of magnitude larger than those for poled PZT-4S and PZT-5H, given by Yarlagadda et al.

7.1 Conclusions

The 3ω measurements themselves were found to be extremely precise—with an error of less than 1%—whereas the TCR measurements had a mean uncertainty of roughly 6%. A major limitation in the TCR measurements was the heating method. The heat was applied from below using a hot plate and the temperature was measured at the specimen heater using a thermocouple. It was found that the thermocouple reading was very sensitive to its location and that the adhesive used to fix the transducer in place tended to lose tack at higher temperatures. This could lead to an overestimation in the TCR and in turn, an overestimate in the thermal conductivity. This could explain the systematic overestimation error of 6% for the thermal conductivity for the fused quartz specimens.

Furthermore, the discrepancy in the fused quartz thermal conductivity measurements could be due to the anomalous staircase behaviour which was observed in all of the 3ω measurements. The size of the "steps" was found to decrease with increasing input power level. This behaviour has never been reported before in the literature.

7.2 Future Work

First, in order to improve the accuracy and precision of the 3ω measurement apparatus, a better method of measuring the TCR is needed. This would be possible by using a precise temperature-controlled furnace. Not only would this homogenise the temperature of the heater and its surroundings, it would also reduce the time required to reach steady-state, since the heat no longer has to flow through the low thermal conductivity specimen to reach the heater. Additionally, the thermocouple would no longer need to be adhered to the heater; therefore, no tampering with the specimen would be required.

Second, further investigation of the anomalous staircase effect is needed to ensure that the measurements are valid, given that this effect has never been reported in the literature. Therefore, further measurements over a wider range of input power levels and with different heater widths are suggested.

Lastly, the initial results obtained for PZT-5A4E—taken in relation to those published in the literature—seem to indicate a correlation between poling, microstructure and thermal conductivity. We are currently investigating the effect of poling on the thermal conductivity of PZT-5A4E. In addition, confirmation of the thermal conductivity measurements made by Yarlagadda et al. on PZT-4S and PZT-5H using the 3ω technique are warranted, given the extremely low values obtained.

References

Abdulagatov, I. M., S. N. Emirov, T. A. Tsomaeva, K. A. Gairbekov, S. Y. Askerov and N. A. Magomedova (2000). "Thermal conductivity of fused quartz and quartz ceramic at high temperatures and high pressures." *Journal of Physics and Chemistry of Solids* **61**(5): 779-787.

Alvarez-Quintana, J. and J. Rodríguez-Viejo (2008). "Extension of the 3[omega] method to measure the thermal conductivity of thin films without a reference sample." *Sensors and Actuators A: Physical* **142**(1): 232-236.

Banerjee, K., G. Wu, M. Igeta, A. Amerasekera, A. Majumdar and C. Hu (1999). Investigation of self-heating phenomenon in small geometry vias using scanning Joule expansion microscopy. Reliability Physics Symposium Proceedings, 1999. 37th Annual. 1999 IEEE International.

Birge, N. O. (1986). "Specific-heat spectroscopy of glycerol and propylene glycol near the glass transition." *Physical Review B* **34**(3): 1631.

Birge, N. O. and S. R. Nagel (1987). "Wide-frequency specific heat spectrometer." *Review of Scientific Instruments* **58**(8): 1464-1470.

Cahill, D. G. (1990). "Thermal conductivity measurement from 30 to 750 K: the 3 omega method." *Review of Scientific Instruments* **61**(2): 802-808.

Cahill, D. G. (2002). "Erratum: ``Thermal conductivity measurement from 30 to 750 K: The 3 omega method" [Rev. Sci. Instrum. [bold 61], 802 (1990)]." *Review of Scientific Instruments* **73**(10): 3701-3701.

Cahill, D. G. and R. O. Pohl (1987). "Thermal conductivity of amorphous solids above the plateau." *Physical Review B* **35**(8): 4067.

Carslaw, H. S. and J. C. Jaeger (1959). Conduction of Heat in Solids. London, Oxford University Press.

Chu, D., M. Touzelbaev, K. E. Goodson, S. Babin and R. F. Pease (2001). Thermal conductivity measurements of thin-film resist. The 45th international conference on electron, ion, and photon beam technology and nanofabrication, Washington, DC (USA), AVS.

Corbino, O. M. (1911). "Periodic variation of resistance of metallic filaments on alternating current." *Atti della Reale Accademia Nazionale dei Lincei* **20**: 222-228.

Corbino, O. M. (1912). "Measurement of specific heats of metals at high temperatures." *Atti della Reale Accademia Nazionale dei Lincei* **21**: 181-188.

DeCarlo, R. A. and P.-M. Lin (1995). Linear Circuit Analysis: Time Domain, Phasor, and Laplace Transform Approaches. Englewood Cliffs, New Jersey, Prentice Hall.

Dubey, G. C., V. K. Srivastava, M. Bal and G. P. Sharma (1991). "Effect of surface roughness on nickel film prepared by sputtering." *Indian Journal of Pure and Applied Physics* **29**(6): 415-17.

Ebeling, H. (1908). "Temperature variation in wires carrying alternating currents." *Annalen der Physik* **27**(2): 391-485.

Erdélyi, A., Ed. (1954). Tables of Integral Transforms. New York, McGraw-Hill.

Gesele, G., J. Linsmeier, V. Drach, J. Friecke and R. Arens-Fisher (1997). "Temperature-dependent thermal conductivity of porous silicon." *Journal of Physics D: Applied Physics* **30**(21): 2911-2916.

Hu, X. J., A. A. Padilla, J. Xu, T. S. Fisher and K. E. Goodson (2006). "3-Omega Measurements of Vertically Oriented Carbon Nanotubes on Silicon." *Journal of Heat Transfer* **128**(11): 1109-1113.

Huang, Y., H. Qiu, F. Wang, L. Pan, Y. Tian and P. Wu (2003). "Effect of annealing on the characteristics of Au/Cr bilayer films grown on glass." *Vacuum* **71**(4): 523-528.

Kallaev, S. N., G. G. Gadjiev, I. K. Kamilov, S. A. Sadykov, Z. M. Omarov and R. M. Ferzilaev (2005). "Thermal conductivity and thermal expansion of ceramics PZT in the region of phase transition." *Integrated Ferroelectrics* **72**: 23-26.

Karl_Suss. (2007). "Karl Suss PH150 Micropositioner." Retrieved August 11th, 2008, from http://www.miller-design.com/karl_suss.htm.

Kim, J. H., A. Feldman and D. Novotny (1999). "Application of the three omega thermal conductivity measurement method to a film on a substrate of finite thickness." *Journal of Applied Physics* **86**(7): 3959-3963.

Lee, S. M. and D. G. Cahill (1997). "Heat transport in thin dielectric films." *Journal of Applied Physics* **81**(6): 2590-2595.

Michalski, L., K. Eckersdorf, J. Kucharski and J. McGhee (2001). Temperature Measurement. Chichester, West Sussex, John Wiley & Sons, Ltd.

Miller, I. and M. Miller (1999). John E. Freund's Mathematical Statistics. Upper Saddle River, Prentice Hall.

Moon, I. K., Y. H. Jeong and S. I. Kwun (1996). "The 3 omega technique for measuring dynamic specific heat and thermal conductivity of a liquid or solid." *Review of Scientific Instruments* **67**(1): 29-35.

Namba, Y. (1970). "Resistivity and Temperature Coeffcient of Thin Metal Films with Rough Surface." *Japanese journal of applied physics* **9**(11): 1326-1329.

Neter, J. and W. Wasserman (1974). Applied Linear Statistical Models: Regression, Analysis of Variance, and Experimental Design. Homewood, Illinois, Richard D. Irwin, Inc.

Paddock, C. A. and G. L. Eesley (1986). "Transient thermoreflectance from thin metal films." *Journal of Applied Physics* **60**(1): 285-290.

Pollock, D. D. (1982). Physical Properties of Materials for Engineers. Boca Raton, Florida, CRC Press, Inc.

Priya, S. (2007). "Advances in energy harvesting using low profile piezoelectric transducers." *Journal of Electroceramics* **19**(1): 167-184.

ProtoConnect. (2006). "Wire Bonding Services." Retrieved August 19th, 2008, from http://protoconnect.com/_wsn/page3.html.

Roundy, S., D. Steingart, L. Fréchette, P. K. Wright and J. Rabaey (2004). Power Sources for Wireless Networks. Proc. 1st European Workshop on Wireless Sensor Networks. Berlin, Germany.

Solarbotics. (2008). "Push Pogo Pin 6 - 6 Point." Retrieved July 23rd, 2008, from http://www.solarbotics.com/products/pp6/.

Taylor, J. R. (1997). An Introduction to Error Analysis: The Study of Uncertainties in Physical Measurements. Sausalito, California, University Science Books.

Touloukian, Y. S., Ed. (1973). Thermal Conductivity: Nonmetallic Solids. Thermophysical Properties of Matter. New York, IFI/Plenum.

Warkusz, F. (1987). "Some transport properties of granular metal films with rough surfaces." *Vacuum* **37**(1-2): 115-118.

Wilson, P. R., J. N. Ross and A. D. Brown (2004). "Predicting total harmonic distortion in asymmetric digital subscriber line transformers by simulation." *Magnetics, IEEE Transactions on* **40**(3): 1542-1549.

Yang, J. (2008). Staff Research Scientist. Warren, Michigan.

Yarlagadda, S., M. H. W. Chan, H. Lee, G. A. Lesieutre, D. W. Jensen and R. S. Messer (1995). "Low Temperature Thermal Conductivity, Heat Capacity, and Heat Generation of PZT." *Journal of Intelligent Material Systems and Structures* **6**(6): 757-764.